東京大学大学院　新領域創成科学研究科
基盤科学研究質系物質系専攻

平成 19 年度
修士論文

The influence of crystal defects on the photoconductivity of $SrTiO_3$

結晶欠陥が$SrTiO_3$の光電気伝導特性に与える影響

2008 年 1 月 29 日提出
指導教員：Mikk Lippmaa 准教授

66106
Yasufumi Urata

The influence of crystal defects on the photoconductivity of $SrTiO_3$

Contents

Chapter 1
General Introduction

Introduction

Electronics devices are indispensable in our lives. The most common material used in modern semiconductor electronics is high-purity Silicon. The Silicon technology has developed rapidly since the construction of the first practical transistors in the early 1950s. Nowadays we find large-scale integrated circuits in almost all electronic instruments, resulting in dramatic advances in industry, biology, medical science, etc.

In the present world, more and more information needs to be dealt with in real time and regardless of location, prompting terminology like 'ubiquitous computing' or 'ubiquitous (information technology) society'. In order to support such ideas, further progress of electronics is necessary. However, limitations of silicon as a foundation for electronics are well known and the limitations are beginning to be felt in practical applications, such as high-speed digital devices, low-power devices, and particularly in high-density storage. Tellingly, mechanical spinning magnetic mass storage has been in use for over 50 years and remains unchallenged by silicon to this day, seriously limiting the ubiquitous nature of high-performance computing. As a solution, attention has turned to enhancing device performance by applying new materials, eventually replacing silicon in certain cases, like storage.

In Traditional semiconductors, like silicon or germanium, applications are limited because, at least close to room temperature, it is 'only' possible to make use of a single degree of freedom, namely electric charge. In contrast, materials like transition metal oxides have several degrees of freedom. In addition to electric charge, it is possible to utilize spin and orbital order. Even when working only with electronic charge, the charge densities that can be controlled in oxides are much higher than in silicon, which is why oxide devices can potentially be downscaled more easily than traditional semiconductors. The other forms of order that are accessible in oxides can lead to a wide range of useful physical properties, such as high-T_c superconductivity in cuprates [1] or colossal magnetic resistance in manganites [2]. It may be expected that the next generation of electronic devices will utilize these types of effects and it is for this reason that I have investigated the transport properties of a prototypical perovskite oxide, $SrTiO_3$.

Perovskite

Perovskite (ABO_3) is a very common structure in transition metal oxides. The atomic positions in a perovskite unit cell are shown in Figure 1-1. Ideally, the unit cell is cubic with the so-called A-site cation at the corner of the cube and the B-site cation at the center of the cube. The oxygen atoms are at the face center of the unit cell surrounding the 6-way coordinated B-site metal. Although the basic structure is cubic, perovskites can accommodate large structural distortions in the form of vacancies and distortions or tilting of the BO_6 octahedra. Such distortions usually accompany electronic phase transitions. The diverse physical properties of perovskites are mainly derived from the *d* electronic states, while the A-site ions form the frame of the crystal and also serve as a source of carriers. Perovskites are layered crystals and there are thus two possible surface terminations for a (001)-oriented crystal: the AO plane and the BO_2 plane.

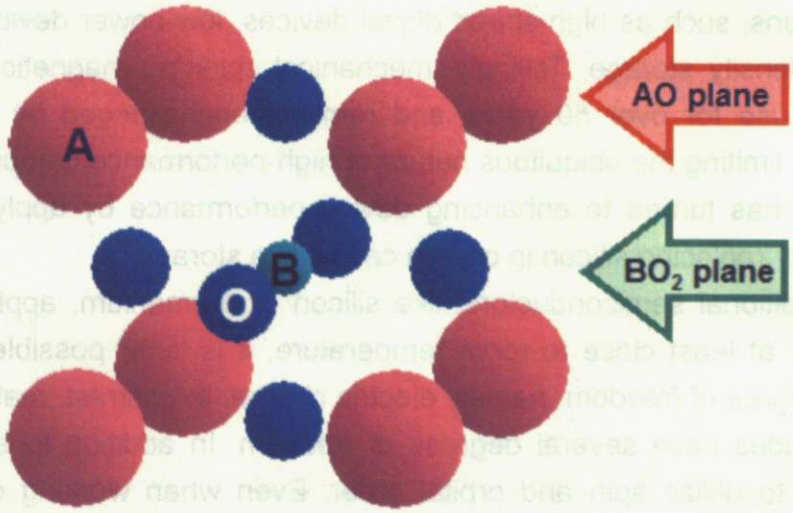

Fig. 1-1 Schematic model of the perovskite structure.

$SrTiO_3$

$SrTiO_3$ has a nearly ideal perovskite crystal structure with a tolerance factor of almost 1, with Sr at the A-site and Ti at the B-site. The lattice constant is 3.905 Å at room temperature [3]. $SrTiO_3$ has been recognized long time ago for its unique dielectric properties, that is, the very large dielectric constant, which increases from

about 300 at room temperature to more than 10000 at low temperature [4]. Unlike other oxides with similar structure, such as $BaTiO_3$, $SrTiO_3$ does not become ferroelectric at any temperature. Instead, it enters a quantum paraelectric state at around 10 K [5]. The ferroelectric state can be induced only by distorting the lattice, either by isotopic substitution [6], application of an electric field [7], or application of stress [8] Depending on doping, $SrTiO_3$ can be a very good insulator, a wide-gap semiconductor, or even a good metal. Superconductivity appears in a carrier concentration range of 10^{19}-10^{21} cm^{-3} [9], but only below 0.3 K.

From the point of view of device construction, it is interesting that the insulator-to-metal transition occurs in $SrTiO_3$ at an unusually low carrier density of about 10^{18} cm^{-3}. For this reason, $SrTiO_3$ can be used in field-effect transistors (FET) and other oxide heterostructures where two-dimensional physics can be explored. For FET, $SrTiO_3$ can be used in bulk form, as it can serve both as a substrate and work as the transistor channel. $SrTiO_3$ substrates with relatively high crystal quality are easily available and it has a good lattice match with many other perovskite-type oxides. $SrTiO_3$-based FETs are majority-carrier devices, where the conductivity is modulated by changing the density of electrons in the channel region. Understanding the mechanisms that influence the transport properties of $SrTiO_3$ is therefore very important for device construction.

Non-doped $SrTiO_3$ is a band insulator with a bandgap gap energy of $E_{gap}\approx3.2$ eV [10]. In order to probe carrier transport in the crystals, carriers have to be injected somehow before measurements can be done. There are several possible methods to inject carriers into $SrTiO_3$, such as impurity doping [11], field effect [12], and photocarrier injection [13]. Impurity doping is the most common technique. It is known that the Hall mobility of chemically-doped $SrTiO_3$ depends on the density of dopants, as shown in Figure 1-2. Impurity doping is not a suitable method for characterizing crystals for device fabrication, since the impurities also create disorder, as witnessed by the mobility drop in highly doped samples. Field-effect doping requires the construction of an FET device. The third method was therefore selected for this work, namely photocarrier injection by ultraviolet light illumination.

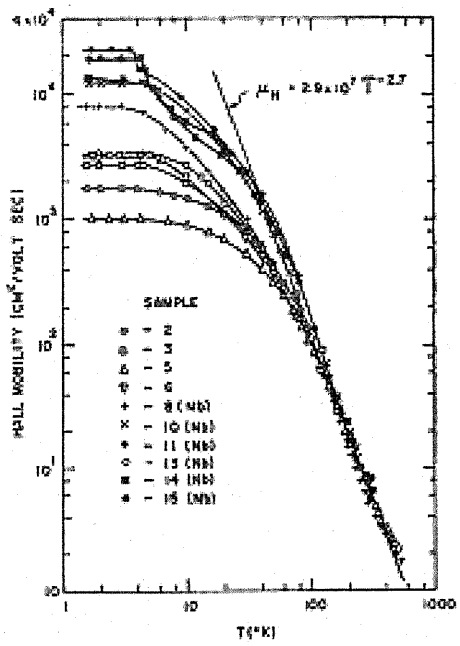

Fig. 1-2 Temperature dependence of Hall mobility of chemically doped $SrTiO_3$ [12].

Photoconductivity

Photoconductivity is a common property for all semiconductors. The merit of photoconductivity measurement is that no permanent lattice defects are created by illumination at moderate intensities. Yasunaga has reported that photo-excited electrons have a very high mobility in $SrTiO_3$ [14]. By illumination with photons that have an energy exceeding the band gap energy of $SrTiO_3$, electrons are excited from the valence band to the conduction band in $SrTiO_3$. Electrons may recombine with holes. The recombination rate affects the carrier concentration, which appears in transport measurements. The dynamic nature of the carriers needs to be considered when using the photoconductivity results to predict the behavior of carriers injected by field-effect doping.

Purpose of this study

The purpose of this study is to investigate the influence of crystal defects on the photoconductivity of $SrTiO_3$. Although the main interest is in field-effect devices, the device performance is affected by the type of substrate crystal used for experiments. For example, nominally non-doped $SrTiO_3$ substrates can have quite different

low-temperature characteristics, indicating that the defect concentrations and possibly the types of defects that are present are different. The differences can result from the growth process, chemical impurities, differences in thermal processing and differences in the mechanical handling of the substrates. It was therefore necessary to devise a simple way of characterizing the transport properties of non-doped crystals before they are used for device fabrication. The technique needed to be experimentally simple, fast, and reliable. For these reasons, a photoconductivity measurement setup was constructed and crystals with several possible defect types were studied.

As seen in Fig. 1, the Hall mobility is lost when the density of impurity-derived crystal defects is increased. In FETs no impurities are intentionally doped into the substrate, but defects can still be introduced as a side-effect of the thin film growth process, significantly affecting the carrier transport. To simulate typical defect formation mechanisms and compare the properties of defect-rich samples with the best available crystals, clean bulk $SrTiO_3$ samples were measured to obtain reference data. To probe the effects of oxygen and Sr vacancies that usually form during high-temperature processing, samples were annealed in oxidizing or reducing environments or grown from nonstoichiometric raw powder mixtures and a photoconductivity investigation was done on those samples. Third, photoconductivity dynamics was investigated to see if it is possible to distinguish the physical mechanism of how carriers interact with defects, i.e. trapping at defect sites.

References

1. J. G. Bednorz et al., Z. Phys. **B64**, 189 (1986)
2. Y. Tokura et al., Phys. Rev. B, **53**, R1689 (1996)
3. K. H. Hellwege, A. M. Hellewege, Science and Technology New Series, Group III, **Vol.16a**, 59 (1981).
4. T. Sakudo and H. Unoki, Phys. Rev. Lett. **26**, 851 (1971).
5. K. A. Müller and H. Burkard, Phys. Rev. **B 19**, 3593 (1979).
6. M.Itoh, R.Wang, Y.Inaguma, T.Yamaguchi, Y-J.Shan and T.Nakamura, Phys. Rev. Lett. **82**, 3540 (1999).
7. J.Hamberger, P.Lunkenheimer, R.Viana, R. Böhmer and A. Loidl, Phys. Rev. **B 52**, 13159 (1995).
8. H. Uwe and T. Sakudo, Phys. Rev. **B 13**, 271 (1976).
9. J.F.Schooley, H.P.R.Frederikse, W.R.Hosler and E.R.Pfeiffer Phys. Rev. **159**, 301 (1967).
10. M.Cardona, Phys.Rev. **A 651**, 140, (1965).
11. O.N.Tufte and P.W.Chapman, Phys. Rev. **155**, 796 (1967).
12. H. Nakamura, H. Takagi, I. H. Inoue, Y Takahashi, T. Hasegawa and Y. Tokura, Appl. Phys. Lett. **89**, 133504 (2006).
13. T. Feng, Phys. Rev. B **25**, 627 (1982).
14. H. Yasunaga, J. Phys. Soc. Jpn. **24**, 1035 (1968).

Chapter 2
Equipment and techniques

Chemical wet etching

It is known that $SrTiO_3$ can be etched by several kinds of acid. The merit of wet etching is that the surface layer can be gently removed without causing physical damage, which is unavoidable when mechanical polishing or grinding is used. In slow etching, the etchant gradually eats the surface of a $SrTiO_3$ crystal from the step edges and is often used to planarize a polished surface to obtain a step-and-terrace surface morphology. Such etching has to be done at a carefully optimized rate to preventing direct vertical etching into flat terrace surface [1]. Long-time etching generally results in the formation of large etch pits, because etchant preferentially dissolves the crystal at defect points on the surface of the crystal.

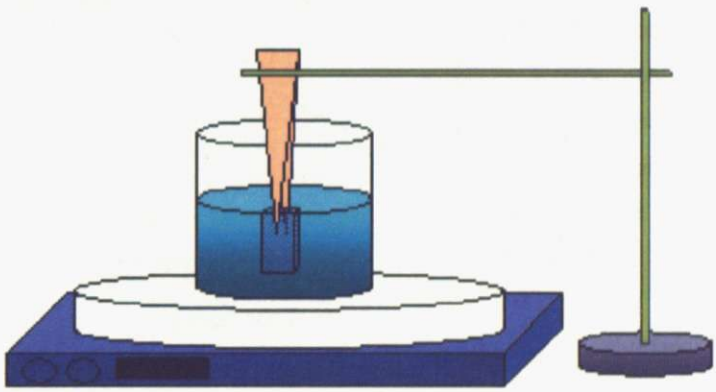

Fig. 2-1 Geometry of the chemical wet etching.

Figure 2-1 shows the geometry of the chemical etching instrument that was used in this study. The chosen acid was 85% phosphoric acid, which can give a reasonably fast etch rate for $SrTiO_3$. A sample was fixed in the acid by tweezers made of zirconia ceramics. The acid was heated on a laboratory hot plate and stirred with a mechanical stirrer in the hotplate. The whole etching setup was

placed in a draft hood. The etching rate is impractically slow at room temperature, but can be accelerated considerably by increasing the temperature of the acid. The temperature was measured with a glass thermometer dipped directly into the acid. As a first step, the etching rate was measured. The rate was estimated by measuring the etching depth after photoresist lines were formed on the surface of a $SrTiO_3$ crystal. Because the etching had to be done at high temperature, it was necessary to hard bake the resist at 150°C. This way the resist pattern survived long enough in the hot acid for the etching experiments to finish. The depth of the etched trenches was measured by the DEKTAK profilometer. Figure 2-2 shows the results of the etching rate estimation. The highest practical acid temperature was 133°C and the etching rate was about 35 nm/min.

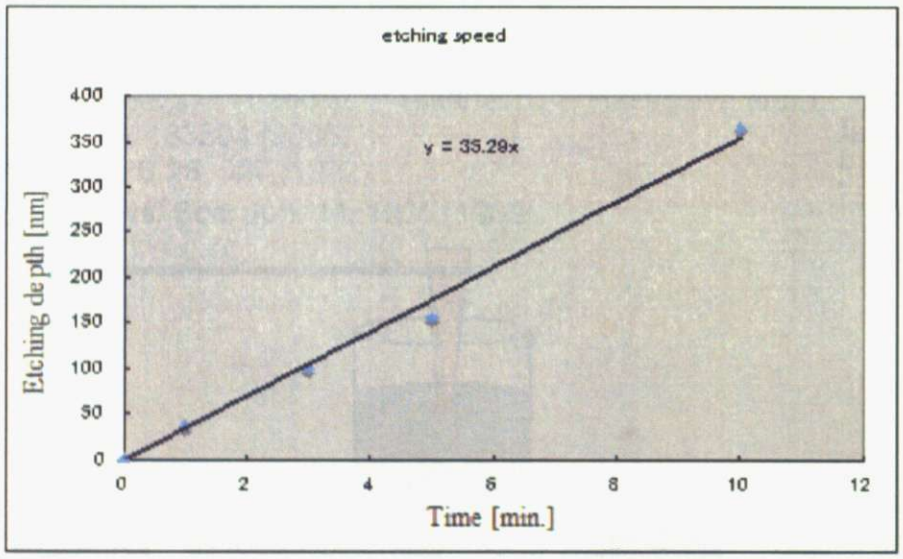

Fig. 2-2 Time dependence of etching depth at 133°C.

Photoconductivity measurement

Figure 2-3 shows the geometry of the photoconductivity measurement system. A sample was attached to the cold finger of a flow-type liquid helium-cooled cryostat (Rockgate co.) and illuminated through a quartz viewport (Edmond optics, 45814-G) with ultraviolet light. Monochromatic light was obtained by

passing light from a 1 kW Xe lamp (Ushio, UXL-1000D) through a double monochromator (Jasco CD-25CD). The monochromator uses a diffraction grating and slits to select a narrow spectral range from the original light. In a double monochromator, essentially two monochromators are attached back-to-back to improve the dispersion, i.e. the spectral purity of the passed light. [2]. Figure 2-4 shows the schematic model of the main optical components inside one half of the double monochromator (Czerny-Turner mount). The operating principle of a monochromator is as follows; Light from a light source is focused on the entrance slit, S1. The diverging input light beam is collimated with a curved mirror M, and directed at a G. In this case, special UV-tolerant gratings were used due to the high intensity of UV light obtained from the 1 kW Xe lamp. The diffracted light provides a spectrum image in the scattering direction, which is centered on slit S2 by another focusing mirror M.

The diffraction equation is

$$k\lambda = d(\sin\alpha + \sin\beta) \qquad (k = 0,\pm1,\pm2....) \qquad (2\text{-}1)$$

By defining *a* as

$$2a = \beta - \alpha$$

and using an angle ϕ, which is the angle between the normal and the bisector of incoming and outgoing light axes, allows the α and β angles to be written as

$$\alpha = \phi - a$$
$$\beta = \phi + a$$

Eq. (2-1) can then be written as

$$k\lambda = 2d\sin\phi\cos a \qquad (2\text{-}2)$$

and λ is proportional to $\sin\phi$. The desired wavelength can be selected by turning the grating, i.e. changing the angle ϕ.

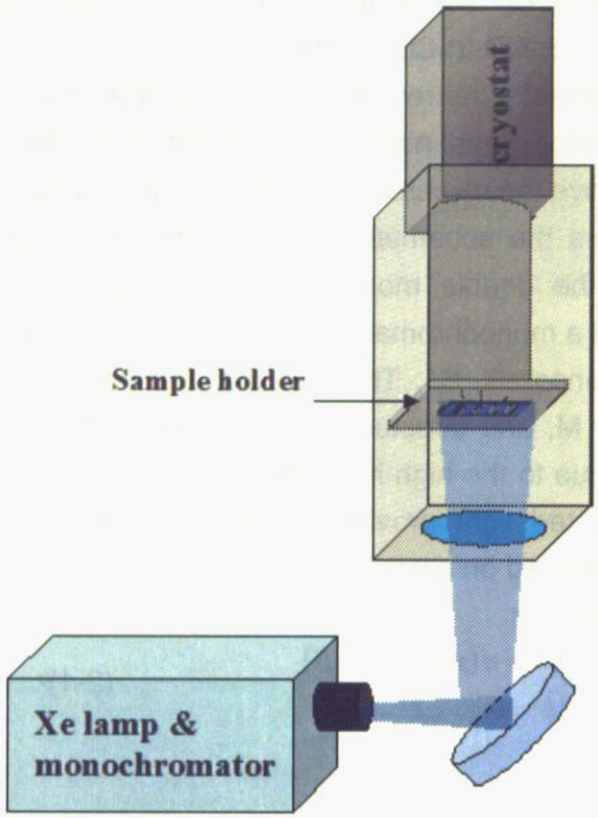

Fig. 2-3 Schematic model of photoconductivity measurement system.

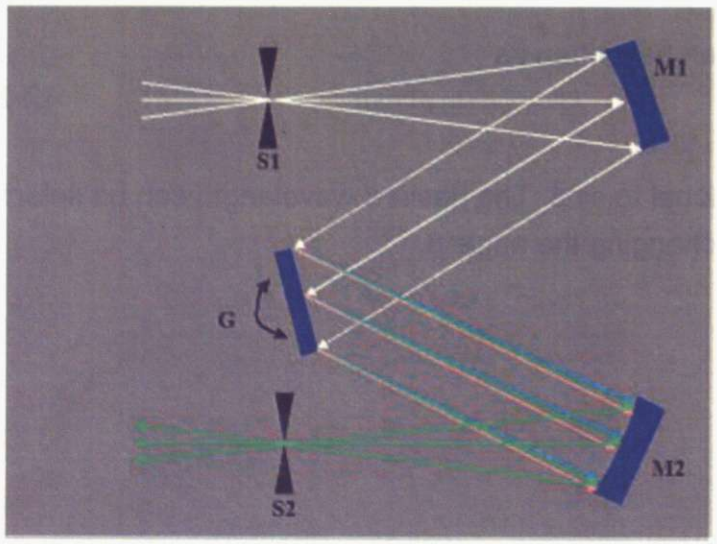

Fig. 2-4 Schematic model of Czerny-Turner mount.

A computerized wavelength scanner is attached to the monochromator that allows the wavelength of the outgoing light to be scanned at an arbitrary rate. The spectral purity of the light can be adjusted by changing the width of the entrance and exit slits of the monochromator. Since in this work the photocurrent is not particularly sensitive to small changes in the incident light wavelength, the slits were generally set at 1 or 2 mm width to obtain the maximum available light intensity. The intensity of the output light could be adjusted by changing the width of the middle slit that separates the two sides of the double monochromator.

The cryostat was fixed vertically on a rack, and a UV-compatible mirror (Thorlabs, BB1-E01) was used to direct the light from the monochromator to the sample. The light intensity was monitored with a calibrated Si photodiode (Hamamatsu, S2281), located close to the exit slit of the monochromator. Light signal pick-off was done with a quartz plate in the beam path.

The photoconductivity measurements were generally done in a 4-point configuration using a Keithley 2410 as a current bias source.

Defect-rich $SrTiO_3$

All $SrTiO_3$ single crystal samples, bot stoichiometric and non-stoichiometric, were manufactured by special order by Shinkosha. All crystals were grown by the Verneuil method. The Verneuil method of crystal growth works as follows. First, the raw material with a suitable precursor ration is prepared in powder form. The powder is gradually dropped down from the tank by using hammer that knocks on a mesh powder doser. The falling powder enters the flame of an inverted oxyhydrogen burner. The raw material powder melts in the flame and is deposited on the surface of a growing rod-like crystal that is supported from the bottom. The main advantage of the method is that crystals with very high melting points can be grown very quickly. Other traditional growth methods, such as growing a crystal from melt, are not practical in case of $SrTiO_3$ due to the high temperature that would be needed. The largest drawback of the Verneuil method is the difficulty of controlling the stoichiometry of the crystal and the relatively large density of defects that are grown into the crystal [3]. Figure 2-5 shows the outline of the Verneuil method.

The samples used in this work included as-supplied nominally stoichiometric $SrTiO_3$ crystals and $SrTiO_3$ samples that were grown from precursor powder

mixtures with several different cation ratios (Sr/Ti= 0.98, 1.00, 1.02, 1.04, 1.06). All samples were sliced and polished as is normal for commercial substrates. Polishing was done one side only and the sample surfaces were etched by Bufferd-HF (BHF). Samples were cut by diamond wheel saw or a diamond cutting machine made by Dr. Ohnishi.

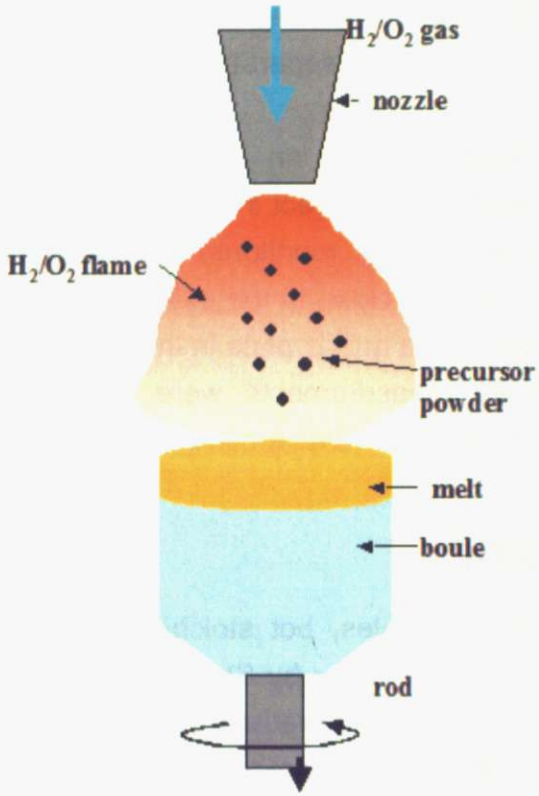

Fig. 2-5 Outline of the Verneuil method of single crystal growth.

Measurement of photoconductivity dynamics

In order to perform time-dependent photoconductivity measurements, an optical chopper (Thorlabs, MC1000A) was set in the optical path between the monochromator and the cryostat. The sample could be illuminated with light chopped at rates between 1 and 100 Hz. In this case, measurements were done in a 2-point geometry with a homemade adjustable bias source and a fast current-to-voltage converter. In order to reduce noise, the bias source used batteries instead of the mains-powered sourcemeters. The current-to-voltage

converter had a variable gain up to 10^9. All instruments were controlled by a computer program written in LabVIEW.

Atomic Force Microscopy

The atomic force microscope (AFM) is a scanning probe microscope. A sharp needle is scanned over the sample surface and the interaction force between the sharp tip and the surface is measured. The resolution of the system is determined by the diameter of the tip and the noise level of the scanner. It is routinely possible to achieve nm order spatial resolution.

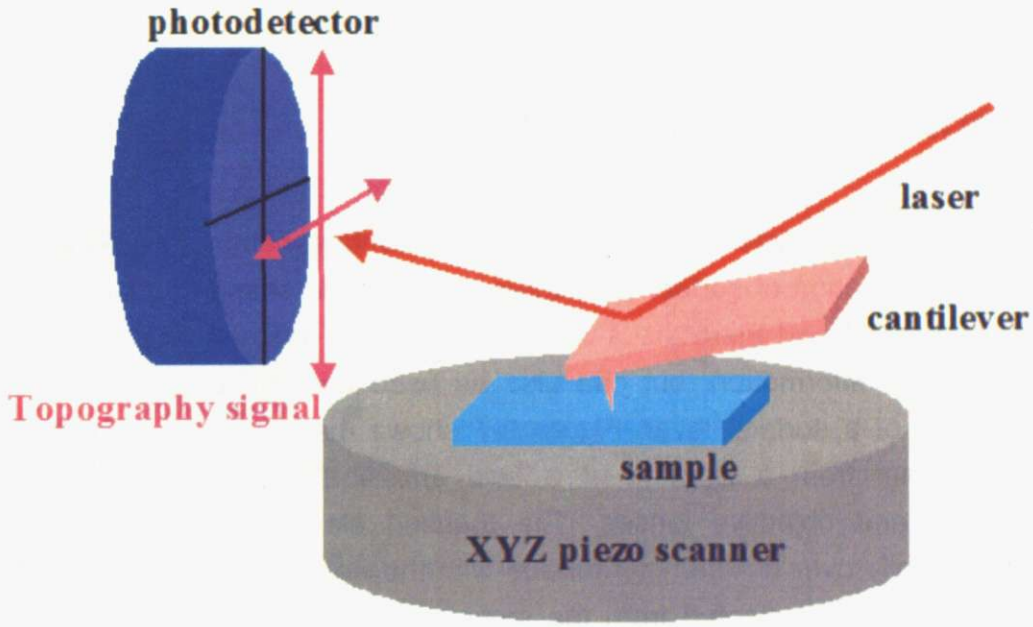

Fig. 2-6 Outline of the atomic force microscope.

In contact mode, the tip at the end of a cantilever is maintained in contact with the sample surface. A laser beam, reflecting from the cantilever surface, is used to determine the bending angle of the cantilever and maintain a preset contact force working point. Knowing the spring constant of the cantilever, it is possible to determine the contact force between the tip and the surface. Angular deflection of the cantilever causes larger angular deflection of the laser beam.

The reflected laser beam strikes a position-sensitive photodetector consisting of four divided photodiodes. The difference between up and down signals indicates the position of the laser spot on the detector and thus the angular deflection of the cantilever. Due to this laser beam deflection method, it is possible to keep the force between a tip and the sample fixed during scan, in the result, topographic image is obtained.

For wide-area scans where the vertical feature heights on the surface can be very large, it is easier to use a different tip position sensing technique. Instead of using an optical deflection measurement, a piezoresistive strain sensor is built into the cantilever itself, allowing direct electrical measurement of tip deflection over a very wide height range. Instruments like this can observe a scan area of up to about 1 square millimeter and is useful for imaging large features, such as device structures or etching features..

Scanning Electron Microscopy

Scanning Electron Microscope (SEM) is a non-contact instrument that is often used for observation of surface structures. Any sample shape can be used for SEM observation and there are a number of imaging modes that can give not only structural information, but can also be used for analyzing the chemical composition of a surface layer. Figure 2-7 shows the outline of a SEM. The electron beam from a filament or a field emission source is gathered by convergent and objective lenses. The focused electron beam is scanned 2-dimensionally over the sample surface with the help of deflection coils. The secondary electrons ejected from the sample are detected with a scintillator, converted to electrical signal, amplified by photomultiplier, and displayed on a computer display.

A drawback of SEM is that the sample has to be moderately conducting. Otherwise the electron beam would charge the sample surface and make observation impossible.

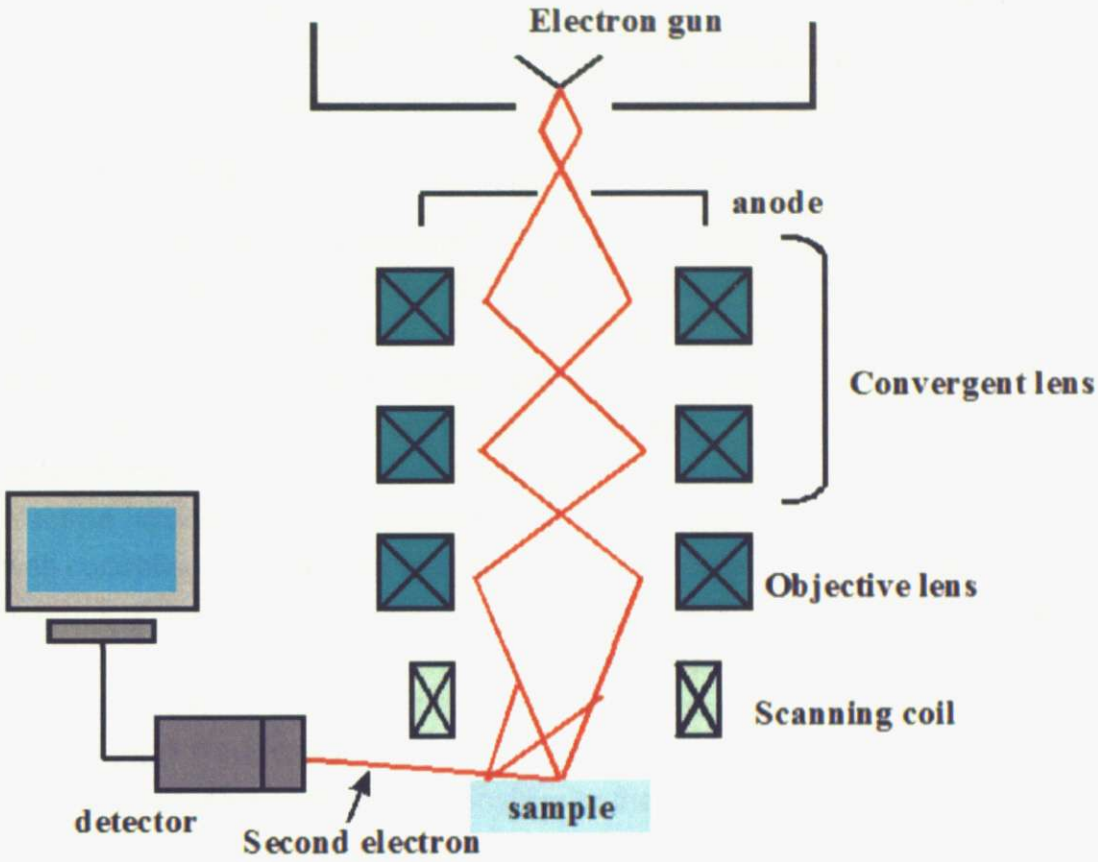

Fig. 2-7 Outline of the Scanning Electron Microscope.

References

1. M.Lippmaa, K. Takahashi, A. Ohtomo, S. Ohashi, T. Ohnishi, N. Nakagawa, T. Sato, M. Iwatsuki, H. Koinuma, and M. Kawasaki, Matt. Sci. Eng. **B56** 111 (1998).
2. 堀場製作所 分光器の原理
3. 日本結晶成長学会, 結晶成長ハンドブック, p540 (1995)

Chapter 3
Influence of crystal defects introduced by the manufacturing process

Introduction

Transition-metal oxides exhibit various potentially useful electronic properties but utilization of these materials in high-quality devices is still very limited in practical applications. One of the main reasons for that is the difficulty of controlling the electrical properties of oxide heterointerfaces. For instance, spin-tunnel junctions of $La_{0.6}Sr_{0.4}MnO_3/SrTiO_3$ show degraded spin ordering due to charge redistribution in the interface layers [1]. Ohtomo et al. demonstrated high electron mobility at heterointerfaces [2]. Heteroepitaxial interfaces with well-controlled electronic properties have the potential to surpass bulk materials in terms of device performance. Understanding the formation of electronic states at oxide heterointerfaces is indispensable for realizing high-performance devices. One approach to understand heterointerface properties is to use field-effect transistors (FETs), which are the most common devices in modern information society, because a FET is very sensitive to the electronic states at the interface between a gate insulator and the semiconducting channel. Figure 3-1 shows the structure of a FET which has been successfully fabricated in this research group previously.

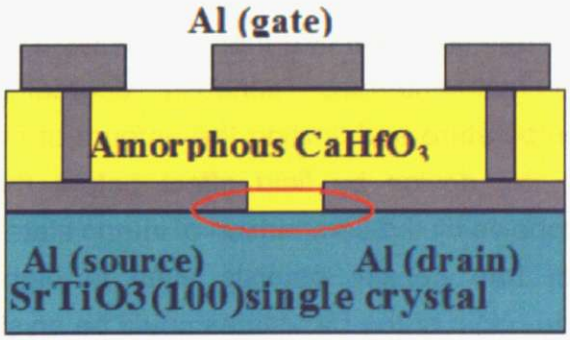

Fig. 3-1 Schematic model of a $CaHfO_3$ gate insulator FET.

In earlier work, the low-temperature performance of $SrTiO_3$ (100) single crystal FETs with epitaxial $CaHfO_3$ gate insulator layers was found to be better than that of FETs with amorphous $CaHfO_3$ gate insulator layers [3,4]. Figure 3-2 shows the energy distribution of trap state density (D_{tr}) below the conduction band edge in bulk $SrTiO_3$. The zero level of the energy scale is set at the mobility edge. In most devices the intrinsic Fermi level is at about 150 meV below the mobility edge.

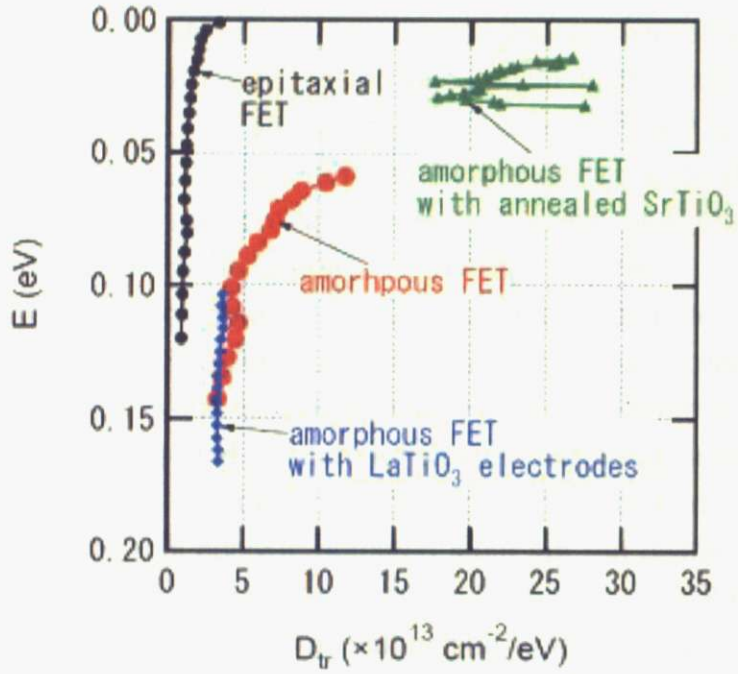

Fig. 3-2 The energy distribution of in-gap trap states of various $SrTiO_3$-based FETs [5].

From those studies, we can conclude that there is always a relatively high trap state density at the heterointerface, seriously degrading the transistor performance at low temperature and limiting the amount of mobile charge that can be introduced in the device by field effect before the gate dielectric breakdown occurs. As shown by the comparison of in-gap state density curves in Fig. 3-2, a significant trap density persists even in high-quality epitaxial interfaces. One possible origin of the trap states could be crystal defects on the surface of the substrate crystal that are caused by the manufacturing process of the single crystal substrates.

High-quality $SrTiO_3$ single crystal substrates are commercially available, but as mentioned in the previous chapter, the crystals are grown by the Verneuil process of flame fusion and therefore the substrate material inevitably contains a relatively high density of lattice defects and contaminants. Since the FET devices used in previous work were macroscopic in size, with typical channel dimensions of $100 \times 500\ \mu m^2$, the device performance could also be affected by mechanical scratches or even deeper damage caused by the slicing of the original boule into wafers and subsequent surface polishing procedures that are necessary for obtaining a well-defined step-and-terrace crystal surfaces. Published reports [6] show that there is a variation of defect density with depth away from the original cut surface in cross-section samples, revealing a very steep dislocation distribution in the skin region of a $SrTiO_3$ substrate. Figure 3-3 shows a transmission electron microscope (TEM) image of the surface region of a $SrTiO_3$ single crystal and the depth dependence of dislocation density of the crystal.

In this study, my aim was to investigate if and how such kinds of defects affect the transport properties of $SrTiO_3$ surface layers that subsequently form the channel of the FETs. This task presented a conceptual dilemma, since non-doped $SrTiO_3$ is a very good insulator and it is therefore impossible to determine the effect that dislocations may have on conductivity without doping the crystal ion some way. Only doping methods that do not affect the defect structure could be considered, and inducing carriers optically was finally chosen. In particular, photoconductivity of defect-rich $SrTiO_3$ crystals was measured. As-received polished samples were compared with those that underwent an additional wet etching treatment that removed a thick, micron-order surface layer.

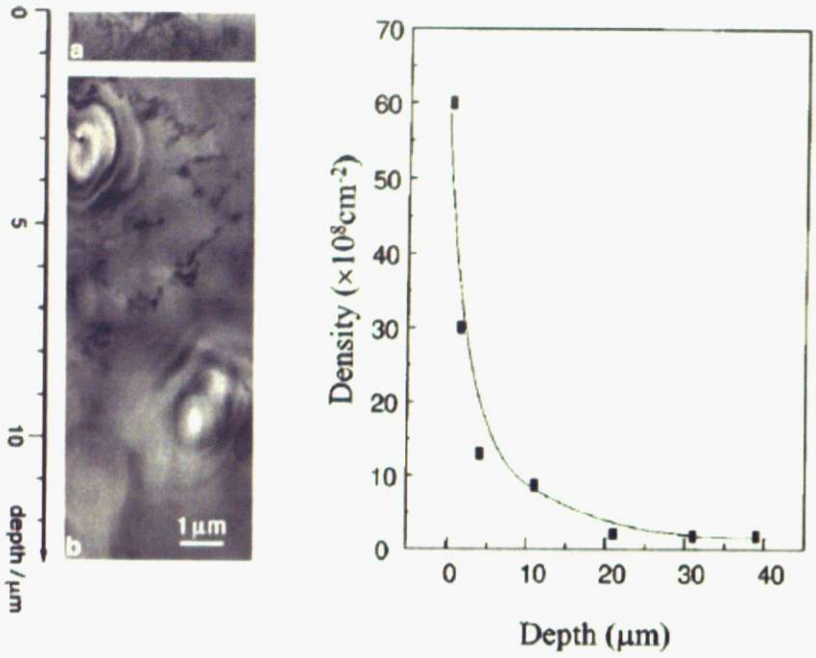

Fig.3-3 (Left) Dislocation distribution (a) at the cut surface and (b) Near the surface of polished $SrTiO_3$. (Right) Dislocation density as a function of depth from the cut surface.

Experimental

The $SrTiO_3$ substrates were obtained from Shinkosha Co. Ltd. Two types of substrates are available from this vendor as standard products: polished substrates and crystals that have been wet etched in buffered HF acid (BHF) to obtain a step-and-terrace surface. The etching depth in the latter case is on the nanometer scale to avoid the formation of etch pits. The substrates were cut into smaller pieces and etched in phosphoric acid (Aldrich, 85%). The etching condition is as I mentioned in chapter 2. The surface of each sample was observed by scanning electron microscope (SEM) and atomic force microscope (AFM, Seiko Instruments Inc., Nanopics 1000). In order to compare crystals that may have different level of damage in the surface layer, several types of samples were prepared: mechano-chemically polished as-supplied $SrTiO_3$, as-supplied $SrTiO_3$ that had been BHF etched, BHF-etched substrates annealed at 1000°C, cleaved surface of $SrTiO_3$, and deeply etched $SrTiO_3$.

$SrTiO_3$ is known to suffer from two main type of defects, oxygen vacancies and Sr vacancies. The former occur when crystals are heated at low oxygen

pressure, which was not done in this study. Sr vacancies form when $SrTiO_3$ is heated under oxidizing conditions, i.e. in air. Microscopic defects could thus be introduced at will by heat treatment of $SrTiO_3$ substrates.

For all samples stripe-shaped Ti electrodes were evaporated on the surface with a pitch of 0.4 mm. The samples were mounted on 44-pin ceramic packages and electrical contact was made to the sample by wire bonding with Al wires (figure 3-4).

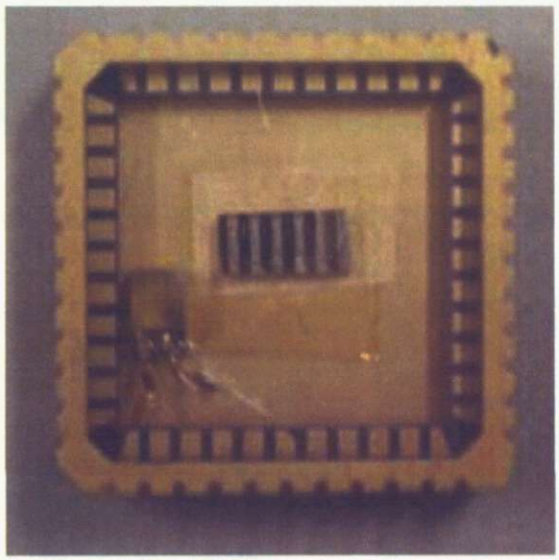

Fig. 3-4 Sample on the ceramics package with silicon diode.

Results and discussion

Figures 3-5 and 3-6 show the SEM and AFM images respectively of the surface of a $SrTiO_3$ substrate that was etched to a depth of 1 μm (temperature is 133 degree, rate is 35.3 nm/ min.). Many circular pits appeared on the surface of the substrate. The diameter of the pits was around a few tens of micrometers. During fast etching, such kinds of pits are etched faster than other flat regions. It is not clear what causes the appearance of the pits, although screw dislocations are potentially one reason.

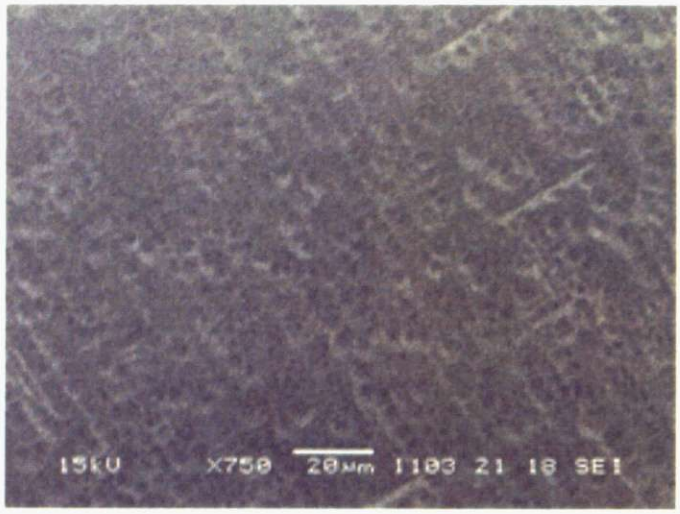

Fig. 3-5 SEM image of surface of $SrTiO_3$ after phosphoric acid etching.

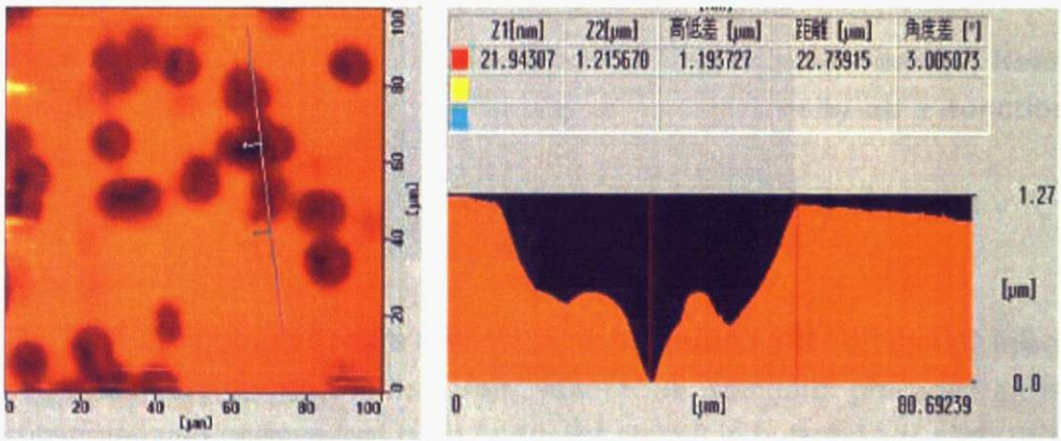

Fig. 3-6 AFM topography image and a cross-section profile of the etch pits on the surface of phosphoric acid-etched $SrTiO_3$

After longer etching, it was possible to remove several micrometers of $SrTiO_3$ from the surface but the number and size of the etch pits increased even further. The temperature dependence of conductance was measured for the as-supplied samples, cleaved crystals, as-annealed, and etched samples. Figure 3-6 shows a comparison the temperature dependence of conductance data below 200 K. The optical excitation was done by illuminating the sample with ultraviolet (UV) light at 320 nm, which corresponds to a photon energy that is well above the band gap of $SrTiO_3$.

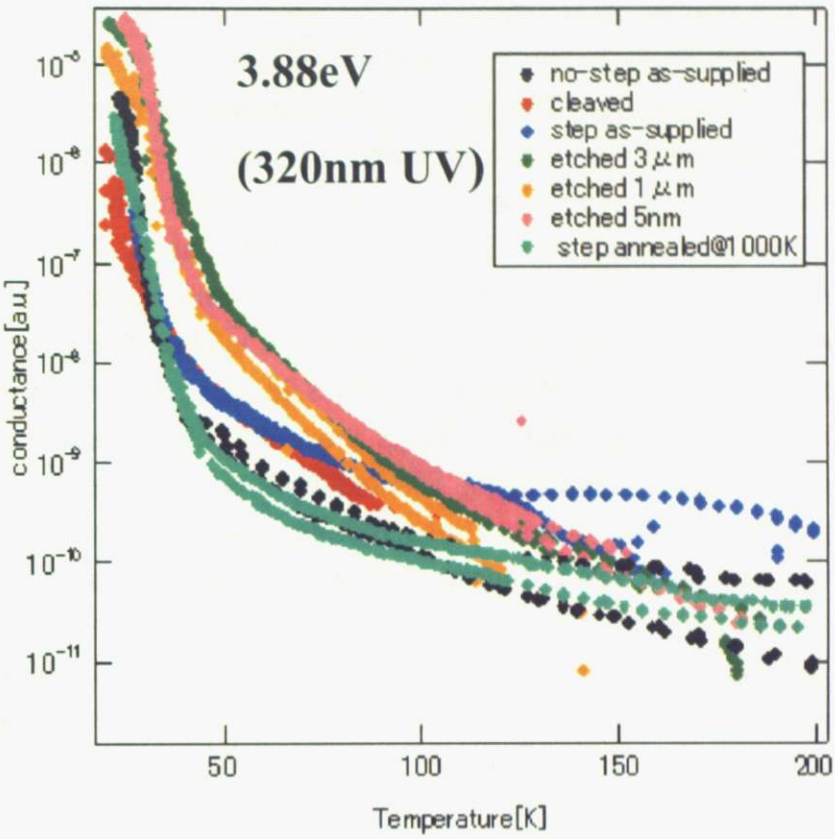

Fig. 3-7 Temperature dependence of conductance of $SrTiO_3$ under 320 nm ultraviolet light illumination.

The absorption coefficient of 320 nm UV light in $SrTiO_3$ is approximately 100 cm^{-1} [7,8], which means that photocarriers are generated only in a thin layer within about 100 nm of the sample surface. As shown in Fig. 3-8, only a small difference could be seen in low-temperature conductivity. However, all samples showed a large jump in conductance at around 30 to 40 K.

The photon energy dependence of conductance was measured for the cleaved surface, non-step as-supplied surface, as-supplied step surface, and annealed step surface. Figure 3-7 shows the conductance plots taken at 150 K and 30 K.

At photon energies between 3.0 and 3.3 eV, a sharp onset of photoconductivity was seen in all samples as expected, since the band gap of non-doped $SrTiO_3$ is 3.2 eV. A distinct band tail is seen in the photon energy dependence of photoconductivity. This type of behavior can be understood if

electronic states exist near the band edge, for example impurity states [9], from where carriers can be thermally excited to the conduction band. The gradual increase of conductivity below the band gap shows that defect states exist to some extent in all samples. This can be considered a common feature for most oxides, as illustrated by the published band tail data in Figure 3-9, which shows the excitation photon energy dependence of photoconductivity of TiO_2 and Al_2O_3. Band tail features were seen in clearly in both cases. A larger detected photocurrent at energies below the band edge energy means that a higher density of in-gap states is present. In figure 3-8, it is clear that only the cleaved surface shows a very low photocurrent below 3.28 eV at 30 K. Crystal defects on the cleaved surface presumably reflects the bulk point defect density of the Verneuil-grown crystals and is not affected by mechanical polishing or other surface processing procedures. These measurements show that the cleaved surface has the lowest defect density while all other samples show a systematic increase. While the increase is small, it corresponds fairly well to the shape of the band tail that was derived from the performance of epitaxial FETs (Fig. 3-2). It is intriguing that there is no detectable difference between polished, etched, and annealed surfaces, indicating that mechanical damage or a moderate density of Sr defects does not have a significant effect on the band tail states.

Conclusion

To investigate how crystal defects affect the photoconductivity of $SrTiO_3$, the temperature dependence and photon energy dependence of photoconductivity was measured. An attempt was made to eliminate surface defects by wet etching and by cleaving. No major differences were seen in the temperature dependence of conductivity, regardless of how the surfaces were modified. This shows that the conductivity is not significantly affected by the presence of mechanical defects or moderate cation segregation, at least in the layer thickness probed by optically induced carriers. In contrast, photon energy dependence of conductivity at low temperature did show that the cleaved surfaces show the lowest density of states in the band tail within about 200 meV of the conduction band edge.

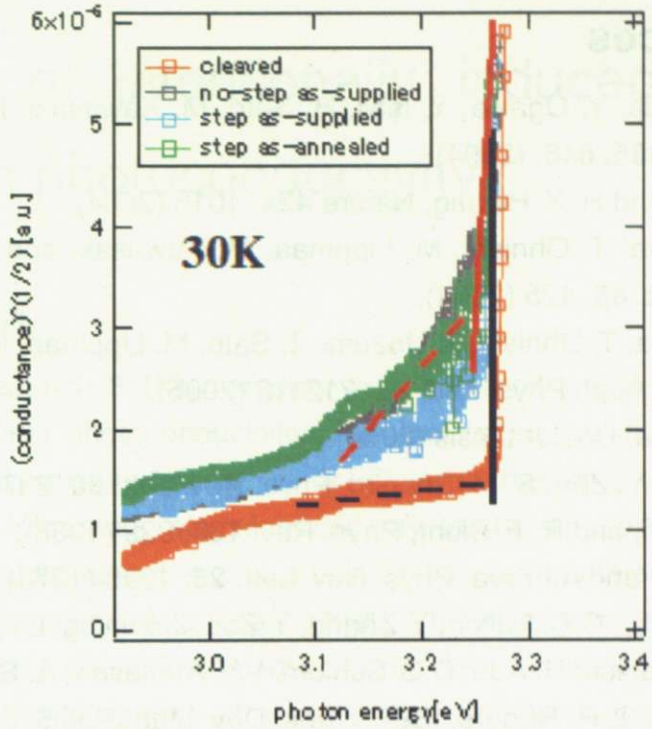

Fig. 3-8 Photon energy dependence of $SrTiO_3$ photoconductivity at 30 K

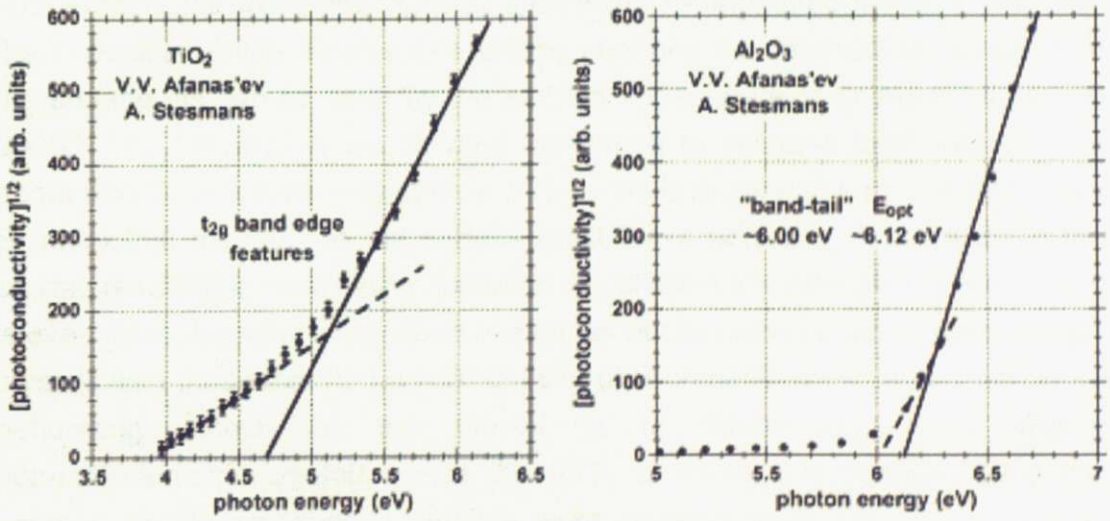

Fig. 3-9 Photoconductivity versus photon energy for TiO_2 and Al_2O_3 plotted to emphasize the weaker features below the strong features that define the onset of strong photoconductivity and optical absorption [7].

References

1. H. Yamada, Y. Ogawa, Y. Ishii, H. Sato, M. Kawasaki, H. Akoh, Y. Tokura, Science **305**, 646. (2004).
2. Ohtomo and H. Y. Hwang, Nature **424**, 1015 (2004).
3. K. Shibuya, T. Ohnishi, M. Lippmaa, M. Kawasaki and H. Koinuma, Appl. Phys. Lett. **85**, 425 (2004).
4. K. Shibuya, T. Ohnishi, T. Uozumi, T. Sato, M. Lippmaa, M. Kawasaki and H. Koinuma, Appl. Phys. Lett. **88**, 212116 (2006).
5. K. Shibuya, Doctor thesis (2006).
6. R. Wang, Y. Zhu, S. M. Shapiro, Phys. Rev. Lett. **80**, 2370 (1998).
7. M.I.Cohen, and R. F. Blunt, Phys. Rev. **168**, 929 (1968).
8. M.Capizzi and A.Frova, Phys. Rev. Lett. **25**, 1298 (1970).
9. G. Lucovsky, C.C. Fulton, Y. Zhang, Y. Zou, J. Luning, L.F. Edge, J.L. Whitten, R.J. Nemanich, H. Ade, D.G. Schlom, V.V. Afanase'v, A. Stesmans, S. Zollner, D. Triyoso, B.R. Rogers, IEEE Trans. Dev. Matt. Rel. **5**, 65 (2005).

Chapter 4
Influence of intentionally induced crystal defects on photoconductivity

Introduction

In this study, defect-rich $SrTiO_3$ samples were prepared in order to study how crystal defects affect photoconductivity. The first technique that was used to induce intentional crystal defects in $SrTiO_3$ was based on generating Sr vacancies in an otherwise stoichiometric crystal by annealing commercial substrates in an oxidizing ambient, i.e. in air. Sr ions segregate on the surface of $SrTiO_3$ upon high-temperature annealing in air. This effect can be seen in Figure 4-1, which shows co-axial impact-collision ion scattering spectroscopy (CAICISS) time-of-flight spectra of a wet-etched $SrTiO_3$ single crystal surface during gradual annealing, starting from room temperature [1].

The time-of-flight spectra show two prominent scattering peaks, corresponding to scattering from Ti and Sr ions in the surface layer of the crystal. At room temperature, the wet-etched crystal is perfectly Ti-terminated, which is why only the Ti peak is visible. Even slight heating changes the chemical composition of the surface, as can be seen by the sudden appearance of Sr signal at around 300°C. The intensity of the Sr peak continued to increase until saturating at about 600°C. Since the only source of Sr is the bulk crystal, it means that every Sr atom that migrates to the surface must leave behind a Sr vacancy in the crystal, resulting in local lattice distortion. By utilizing this annealing effect, which is even more dramatic when done in air, I set out to compare as-supplied $SrTiO_3$ crystals with those that had a high density of Sr vacancies. Another method for generating defects in the crystal is to intentionally grow slightly non-stoichiometric crystals where the Sr/Ti cation ratio is changed by a few percent. To do so, special crystals were ordered from the crystal vendor, Shinkosha.

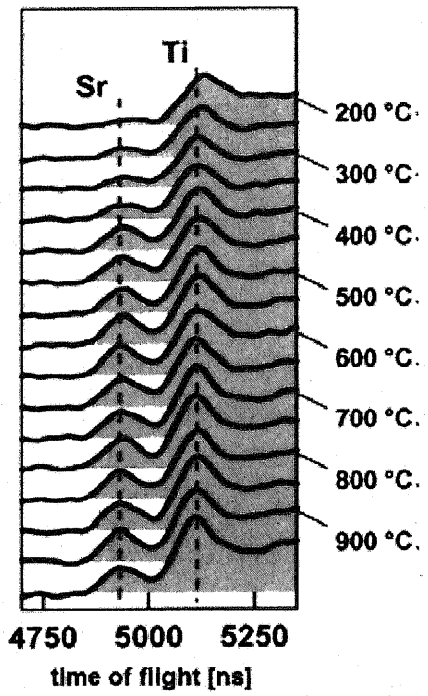

Fig. 4-1 Time-of-flight spectra of the as-supplied wet-etched $SrTiO_3$ substrate surfaces measured *in situ* while heating in vacuum.

The crystals were grown by the same Verneuil process as all the other crystals used in this work, except for using a different Sr/Ti ratio in the source powder for each test boule.

Measurement

The Sr-deficient $SrTiO_3$ single crystals were prepared by annealing at 1000 and 1400°C in a furnace in air. The Sr/Ti ratios used in the non-stoichiometric crystals grown by Shinkosha were 0.98, 1.00, 1.02, 1.04 and 1.06. These numbers refer to the source powder composition, which is not exactly the same as the final cation ratio in the boule. As a general rule, a loss of a few percent of Sr can be expected to occur in the Verneuil growth process. The crystals were cut into approximately 2 mm x 5 mm pieces and stripe-shaped Ti electrodes were evaporated on the surface. The Ti electrodes were 0.4 mm wide and were spaced 0.4 mm apart. The samples were fixed on ceramic chip carriers with varnish. Electrical contact to the Ti electrodes was made by ultrasonic wire

bonding with Al wires. The crystal surface topography was observed by AFM (Shimadzu). A flow-type cold-finger cryostat with an optical window was used for low-temperature measurements as mentioned in Chapter 3. The ultraviolet light source was a 1 kW Xe lamp, while the desired wavelength was selected with a CT-25CD double monochromator. Light intensity was monitored after the monochromator with a calibrated Si photodiode (Hamamatsu). The maximum light intensity at the sample position at 360 nm wavelength was estimated to be 0.01 mW/cm^2.

Results and discussion

Figures 4-2 and 4-3 show AFM images of $SrTiO_3$ crystals annealed at 1400°C for 4 and 12 hours. The AFM measurements were done in tapping mode and the tip oscillation phase shift was recorded simultaneously with the topography measurement. The phase shift signal is sensitive to the chemical composition of the surface, similar to friction-mode measurements. Brighter and darker regions were appeared on the surface after the 4-hour anneal. This pattern is characteristic of surface Sr segregation. A clear stripe pattern was seen after a 12-hour anneal in the phase image, clearly showing that two chemically distinct regions are present on the surface. A particularly dramatic illustration of the segregation process can be seen in the wide-area image in Fig.4-3, where a single large hillock is visible in the center of the scan area. There are radial step edge lines around the particle, indicative of long-range migration of surface material. It is known that such features are cause by the segregation of Sr, forming pyramids of SrO_x on the surface during high-temperature annealing. Re-formation of the crystal can occur, forming a Ti-rich layer near the surface of the crystal. Such particles were not seen on the surface of the same sample after the initial anneal below 1000°C in air. Figure 4-4 shows the results of step height analysis of the $SrTiO_3$ crystal annealed at 1400°C. The height of each step nearly coincides either with the height of one molecular layer of $SrTiO_3$ (4Å) or one atomic layer (2Å). The TiO_2 layer was exposed on the surface after Sr had collected in pyramids on the surface.

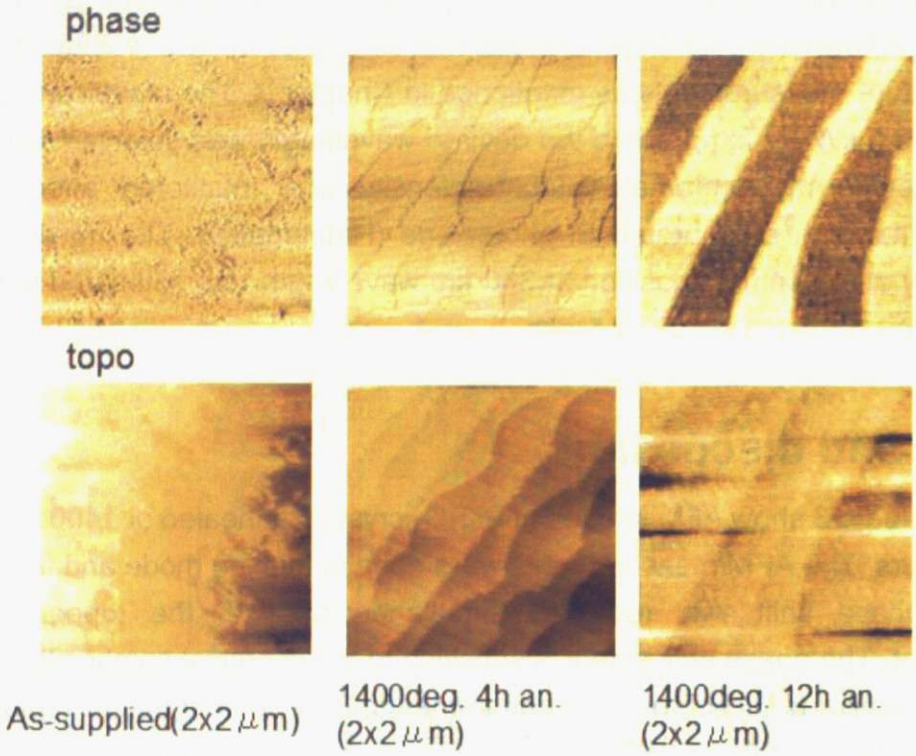

Fig. 4-2 AFM phase and topography images of a $SrTiO_3$ crystal annealed at 1400°C. Scan area is 2×2 μm^2.

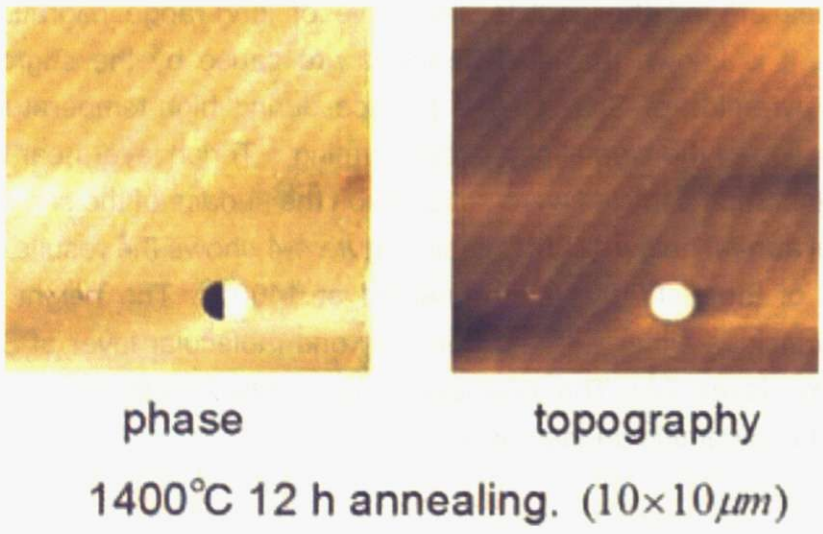

Fig. 4-3 AFM phase and topography images of $SrTiO_3$ annealed at 1400°C. Scan area is 10×10 μm^2.

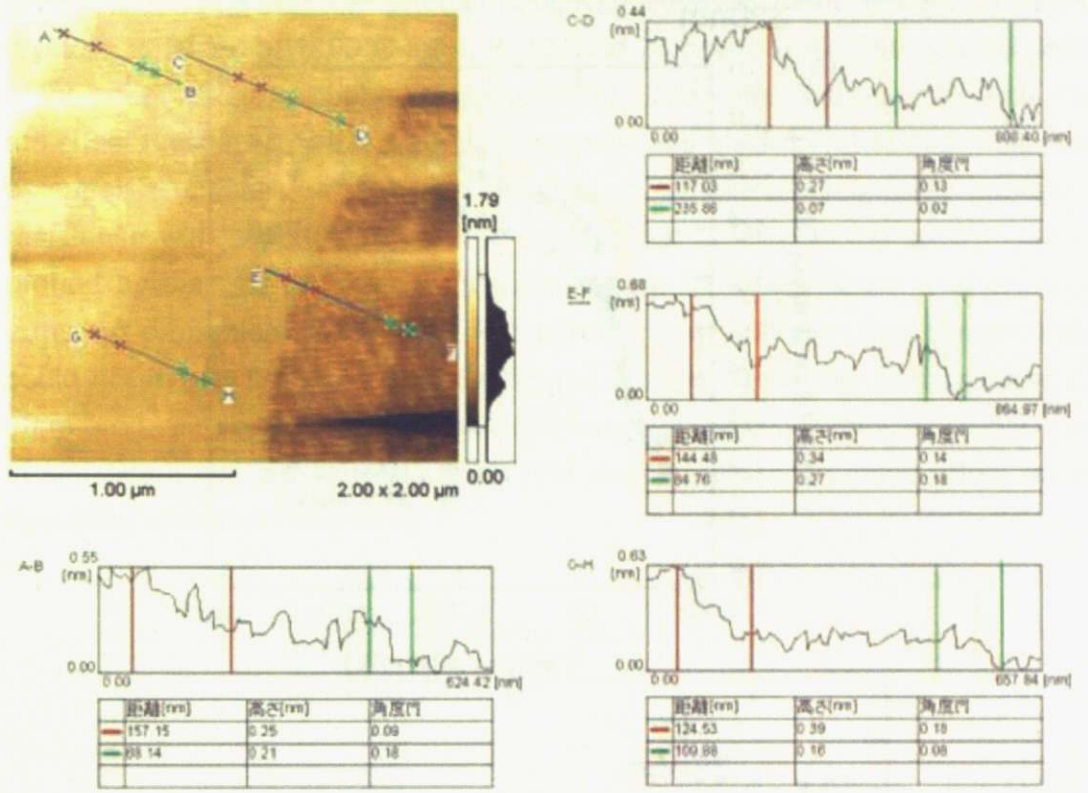

Fig. 4-4 Step height analysis of $SrTiO_3$ annealed at 1400°C.

Figure 4-5 shows the results of the low-temperature photoconductivity measurements of the annealed samples. As-supplied $SrTiO_3$ crystals were compared with those annealed at 1000 and 1400°C for 4 hours in air. The wavelength of light used for carrier injection was either 320 or 360 nm. These two wavelengths were selected because the penetration depth of light changes rapidly close to the onset of band-to-band absorption at around 380 nm. At 360 nm, where the penetration depth is around 1 µm, no difference was seen in the temperature dependence of photoconductivity. In contrast, when 320 nm light was used, with a penetration depth of less than 100 nm, the results are different between the three samples. This result suggests that the segregation of Sr only affected a very thin surface layer of $SrTiO_3$. The defect-rich samples produced by annealing always showed a higher sheet resistance, consistent with the presence of a high density of defects in the crystal

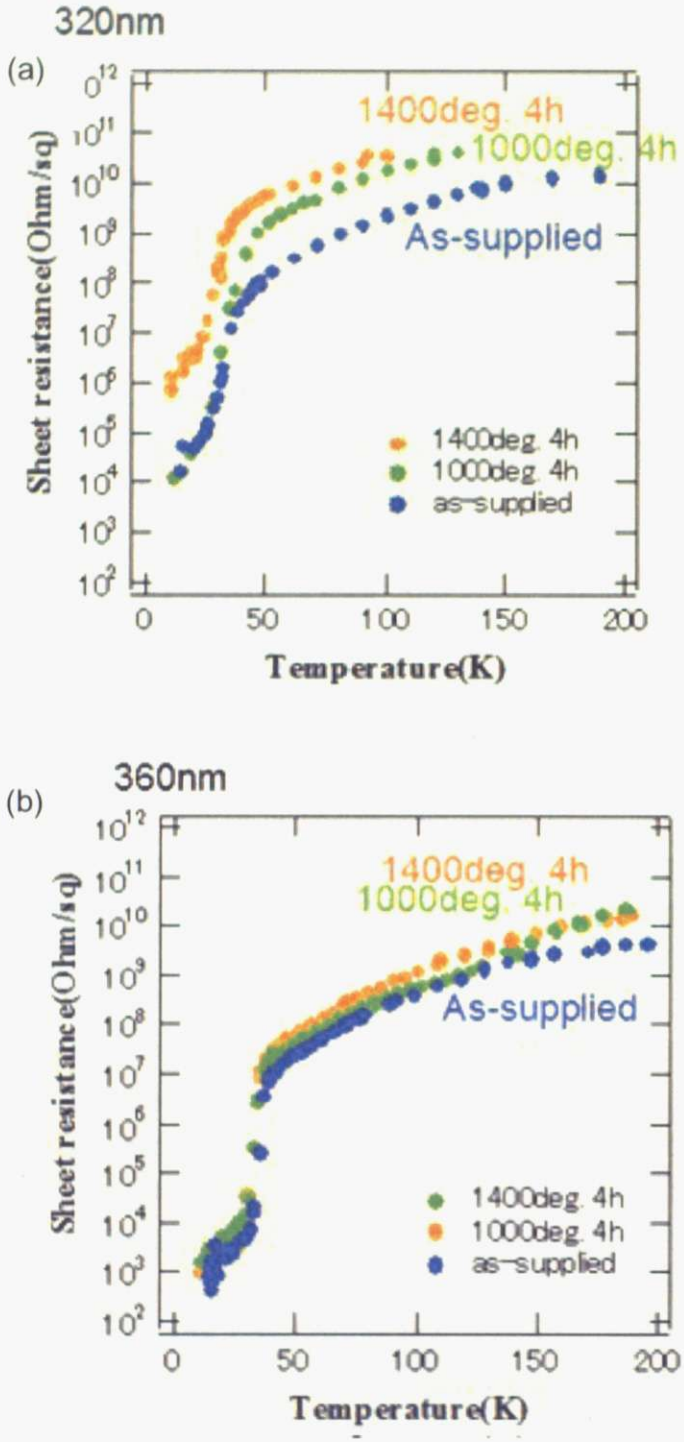

Fig. 4-5 Temperature dependence of sheet resistance of annealed $SrTiO_3$ under (a) 320 nm and (b) 360 nm illumination.

Figure 4-6 shows the photoconductivity measurement results of $SrTiO_3$ crystals annealed at 1400°C for 4, 8, 12, and 24 hours in air. The general shape of the sheet resistance behavior is similar for all samples. Although it is clear that the sheet resistance of the annealed samples was always higher than that of the as-supplied crystals, it was not possible to obtain a systematic change in resistance with annealing time. It is evident that at least in the layer thickness probed by the 320 nm optical excitation, there is no significant change in the transport properties of $SrTiO_3$ at low temperature. Although this measurement could not rule out more dramatic changes in a much thinner surface layer, i.e. 10 m order, it appears to show that high-temperature processing does not result in significant damage to the crystal that would have a dramatic effect on the operation of devices like FETs.

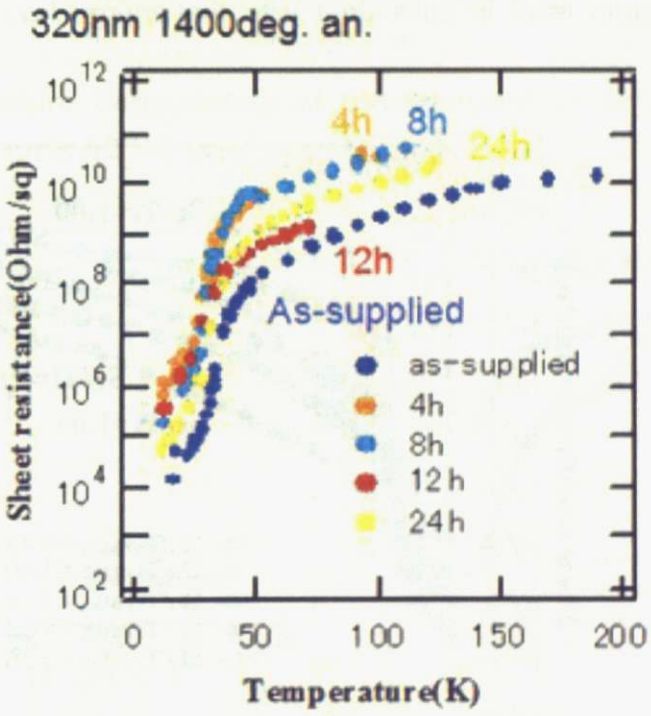

Fig. 4-6 Temperature dependence of sheet resistance of annealed $SrTiO_3$ for several different annealing times.

In an attempt to find a relation between the crystal defects and photoconductivity, $SrTiO_3$ bulk crystals were grown from non-stoichiometric source powder

mixtures. Figure 4-7 shows the temperature dependence of sheet resistance of the non-stoichiometric samples under 360 nm illumination.

All samples showed a sharp resistance change at around 30 to 40K, as did other etched and annealed samples. An additional kink was seen only in the sample made from Sr/Ti=1.00 powder. It should be noted that the stoichiometric source powder composition likely resulted in a slightly Sr-deficient crystal. Empirical tests show that the sample grown from a Sr/Ti=1.04 powder is likely to have nearly ideal stoichiometry. Indeed, that sample shows the lowest sheet resistance over the whole temperature range.

Feng has reported similar behavior, as shown in Fig. 4-8 [2], suggesting that such a sharp change in current over a narrow temperature range is caused by thermal freeing of holes trapped at sensitizing centers. Feng concluded that a dramatic effect on the recombination rate of photocarriers would occur when the hole demarcation level is coincident with the energy level of the sensitizing centers.

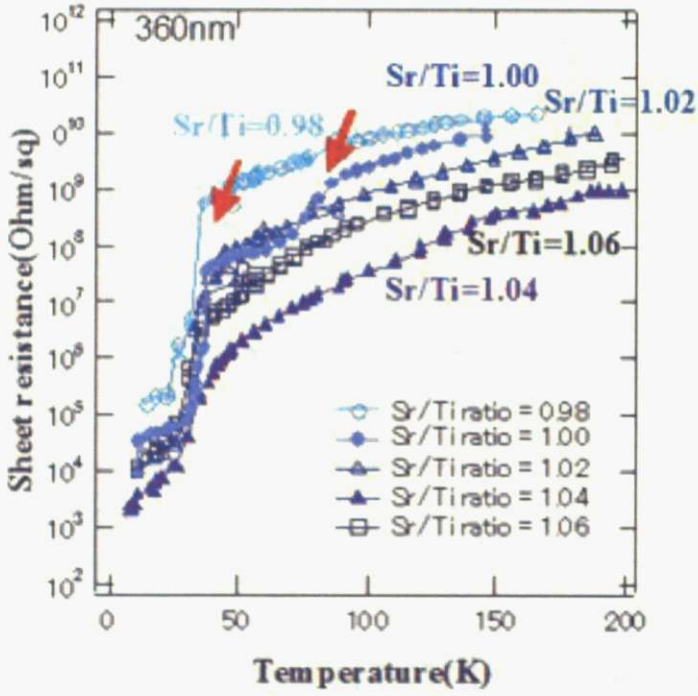

Fig. 4-7 Temperature dependence of the sheet resistance of non-toichiometric $SrTiO_3$ crystals. The compositions of the raw material powders is shown for each samples. Red arrows point to the two kinks seen only in the Sr/Ti=1.00 sample.

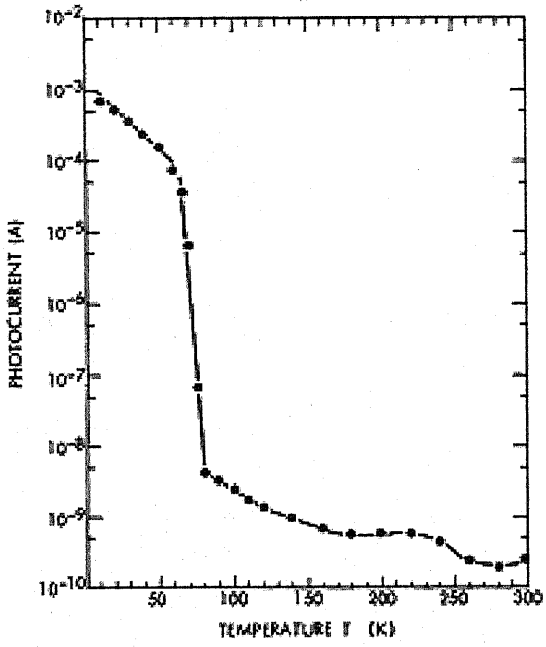

Fig. 4-8 Temperature dependence of photocurrent in $SrTiO_3$. The light intensity was about 5×10^{-7} W / cm^2 sec [2].

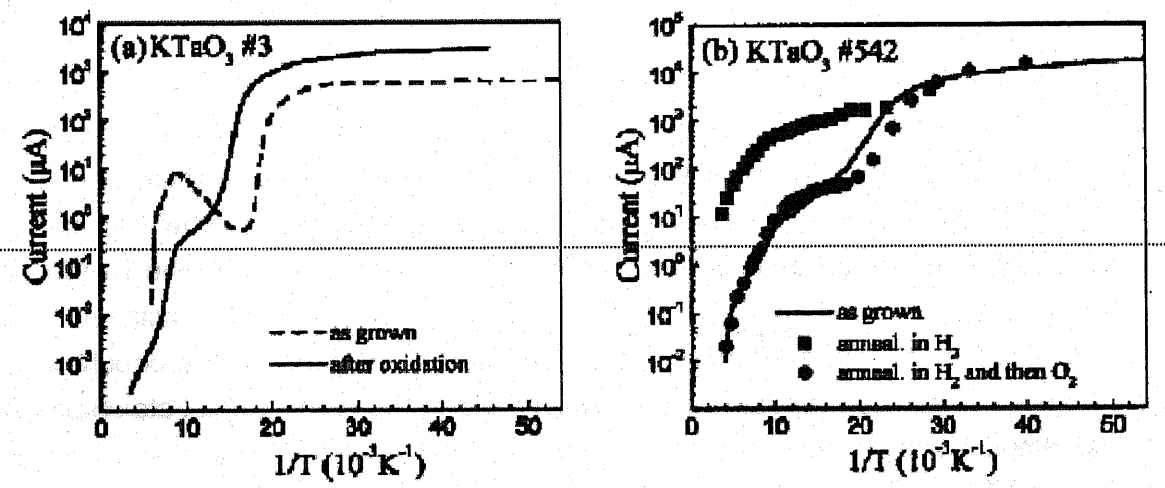

Fig. 4-9 Temperature dependence of photocurrent of $KTaO_3$. The excitation wavelength was 335 nm. Dark resistivities of the #3 and #542 sample were on the order of 10^{14} Ωcm and 10^6 - 10^8 Ωcm respectively at room temperature [3].

Laguta et al. have measured the photoconductivity of $KTaO_3$ [3], as shown in Figure 4-9. In this material, O^- centers can play a special role in the sharp enhancement of photocurrent at low temperatures. It is thus probable that also in $SrTiO_3$, oxidation and reduction can affect the behavior of the photocarriers, just like in the closely related oxide system of $KTaO_3$.

In this case, it is reasonable to assume that the amount of oxygen-related defects is different in the nonstoichiometric crystals. Similarly with the $KTaO_3$ case it appears that another defect level that controls thermal freeing of trapped holes may appear or disappear also in $SrTiO_3$. Among the samples studied in this work, only the sample with a Sr/Ti raw material ratio of 1.00 showed such a double-kink structure. Based on photoconductivity measurements alone, it is not possible to identify which defect level is responsible. It is known that there is a small amount of non-controllable variation between the Verneuil-grown bulk crystals, even when grown under nominally identical conditions. It is thus likely that the Sr/Ti=1.00 sample had a different defect structure from other samples, but no further effort was made to analyze the microstructure of this particular sample due to the apparent lack of sufficient process parameter control during the crystal growth.

The Sr/Ti ratio of raw material used for growing stoichiometric $SrTiO_3$ crystals is around 1.02~1.04. The absolute value of sheet resistances of all bulk samples at 100 K is compared in Figure 4-10. Crystal defects create shallow trap centers and recombination centers, which affects the carrier density in the conduction band and the drift mobility. Higher defect density therefore results in higher resistance. In Fig. 4-10, the lowest value sheet resistance value occurs in the Sr/Ti = 1.02~1.04 range, which is correspond to the experimental stoichiometric composition.

It is also interesting to look at the height of the resistivity jump at around 35K in the low-temperature plots. The resistance ratio between 20 K and 40 K are shown as a function of raw powder composition in Fig. 4-11. Since the height of the transition presumably probes hole localization at defect sites, it is not surprising that the minimum again occurs at a point that corresponds to a stoichiometric crystal that would be expected to have the lowest defect density. The plot is therefore similar to the one in Fig. 4-10.

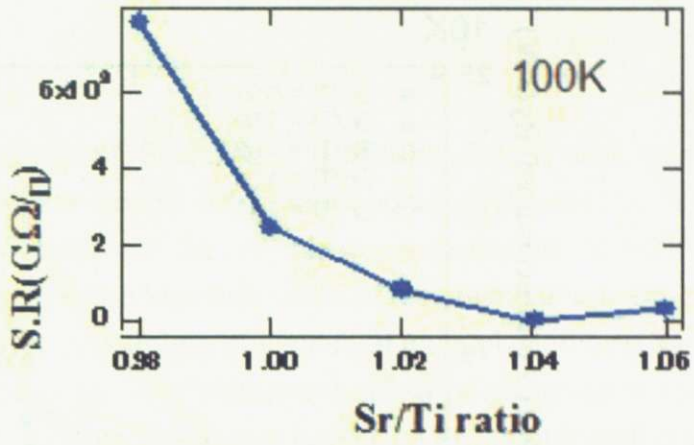

Fig. 4-10 Composition ratio dependence of absolute value of sheet resistance at 100 K.

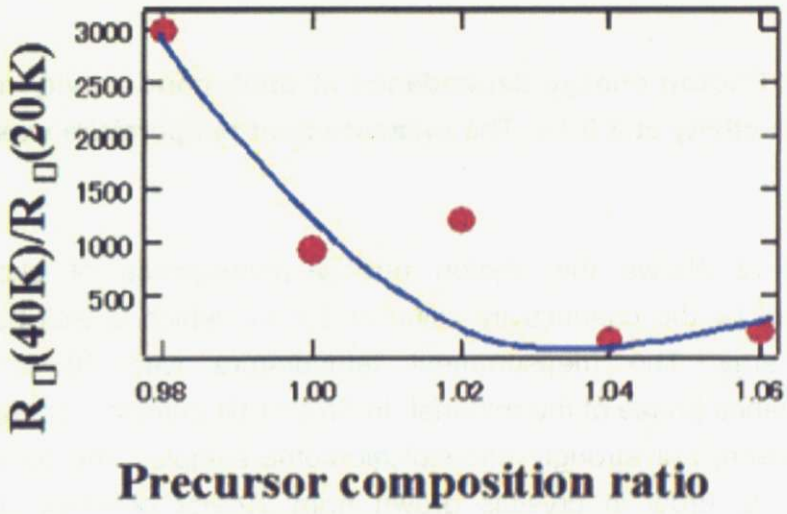

Fig. 4-11 Composition deviation versus sheet resistance ratio at 20 K and 40 K.

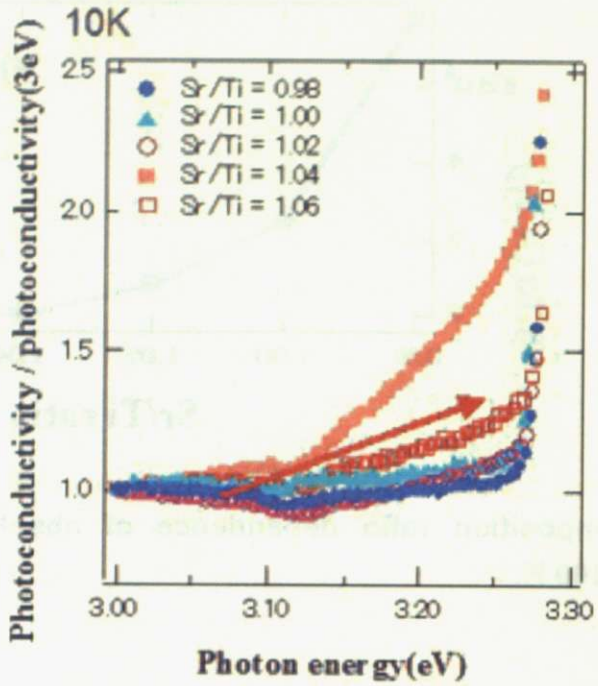

Fig. 4-12 Photon energy dependence of photoconductivity normalized by the conductivity at 3.0 eV. The measurement temperature was 10 K.

Figure 4-12 shows the photon energy dependence of photoconductivity normalized by the conductivity value at 3.0 eV, which is well below the band edge energy. The measurement temperature was 10 K, probing the low-resistance phase of the material. In Sr/Ti=1.04 sample plot, the largest band tail was seen. For strongly non-stoichiometric samples, the band tail intensity appeared to grow in crystals grown from Ti-poor powders. This band tail behavior appears to be in conflict with the observation that stoichiometric crystals have smaller band tails. Indeed, the same Sr/Ti=1.04 sample has the lowest resistance. One possibility is that the photoconductivity measurement only probes defect states near the band edge, and the effect of deeper defect states is only indirectly observed. For further investigation, it would be necessary to identify the types of defects that are created by controlling precursor composition ratio of $SrTiO_3$ but that task would be well beyond the scope of this work.

Conclusion

The photoconductivity of Sr-deficient annealed $SrTiO_3$ was compared with samples that were expected to be strongly nonstoichiometric in order to study the influence of defects on the transport properties of $SrTiO_3$. Systematic differences were seen in the absolute value of resistance and in the height of the sharp change of resistivity among the series of nonstoichiometric samples.

Assuming that the onset of photocurrent at low temperature is caused by the thermal freeing of trapped holes, the height of the photoconductivity jump at around 35 K should be a good indicator of the defect density in the crystal. Photoconductivity can thus be used as a relatively simple technique for selecting crystals with lower defect densities for field-effect doping studies.

references

1. T. Ohnishi, K. Shibuya, M. Lippmaa, D. Kobayashi, H. Kumigashira, M. Oshima, and H. Koinuma, , Appl. Phys. Lett. **85**, 272 (2004).
2. T. Feng, Phys. Rev. B **25**, 627 (1982).
3. V. V. Laguta, M. D. Glinchuk, I. P. Bykov, A. Cremona, P. Galinetto, E. Giulotto, L.Jastrabik and J. Rosa, J. Appl. Phys., **93** 6056 (2003).

Chapter 5
Photocurrent dynamics and dielectricity of $SrTiO_3$

Introduction

In previous Chapters, $SrTiO_3$ samples were measured under static light illumination, where the wavelength was changed, but the intensity was constant in time. On the other hand, it is known that photoconductivity is governed by a dynamic balance between several processes, such as photocarrier generation, recombination, trapping, etc. These processes are affected by the presence of crystal defects, which change the balance of the competing processes, and thus also the static conductivity discussed earlier. In order to obtain a better understanding of the photoconductivity mechanism, it is therefore important to look at the dynamic response of a crystal to ultraviolet illumination. For example, in semiconductors that have large defect densities, like CdSe, it is known that there is a very slow photocurrent response to light illumination [1]. The model that is used to explain such behavior assumes that at the start of a light pulse, the photoexcited carriers are immediately captured by trap sites, and carriers therefore cannot contribute to conduction. Only when the trap sites are filled and a balance is reached between the trapping and detrapping or recombination processes, the photoconductivity reaches a steady-state value. Similar models exist to explain the observed photoconductivity decay curves at the end of a light pulse. Murphy has simulated the ZnO decay curve in order to obtain the trap state energy [2]. My purpose in this work was to use time-dependent photoconductivity measurements and study the possibility of observing the effects that crystal defects have on the dynamics of photocarrier formation and trapping. $SrTiO_3$ should be a good material for such studies, since it is known that many defects are created in the Verneuil crystal growth process.

Wile defect-rich semiconductors can be used as model systems to understand the photocarrier formation and trapping mechanisms, it is also necessary to consider the dielectric properties of $SrTiO_3$, which are radically different from

those of traditional semiconductors. Although $SrTiO_3$ is structurally very similar to well-known ferroelectrics like $BaTiO_3$, it is known to remain paraelectric at all temperatures [3]. Müller and Burkard measured the temperature dependence of the dielectric constant down to 0.3K and even to 0.035K for one sample [4]. A quantum paraelectric phase with constant permittivity below 10 K was observed. The ferroelectric transition temperature of this crystal is so low that a transition to a static polar state is suppressed by quantum fluctuations. Recently, a large enhancement of the dielectric constant of $SrTiO_3$ under UV light illumination was found by Takesada [5]. The enhancement of the static dielectric constant has been suggested to come mainly from a sextic anharmonic oscillator coupled with the photo-induced electrons [6]. In this chapter, I would like to discuss the effects that phonons may have on photoconductivity.

Measurement

A mechanical optical chopper was mounted in the light path between the monochromator and the cryostat. The sample could be illuminated with pulsed light at frequencies from 1 to 100 Hz with a 1:1 dark-light ratio. Stripe-shaped Ti electrodes were evaporated on the $SrTiO_3$ single crystal samples. For high-resistance measurements, 2-point measurements were done and the detected current was amplified with a home-made current-to-voltage converter. Battery-powered electronics was used to avoid line-frequency noise in the measurement. The light intensity was measured with a calibrated Si photodiode.

In addition to conductivity, the capacitance of $SrTiO_3$ was also measured. In capacitance measurements, a 90 nm-SiO_2 and 30 nm gold layer was evaporated on both sides of a double-side polished $SrTiO_3$ substrate (Shinkosha). The single crystal was cut down to 2.2×4.4 mm^2 size. The sample was fixed on a ceramic chip carrier package with silver paste. Al wires were connected to the top of the sample and the surface of the ceramic package. Figure 5-1 shows the geometry of the capacitance measurement. A silicon diode was also set on the package to measure the sample temperature. The sample was set in the same cryostat as described in previous Chapters. The dielectric constant of the sample was calculated from the sample capacitance, measured by four-terminal method with a precision LCR meter (Agilent, 4284A). The light source was a Xe lamp as described previously.

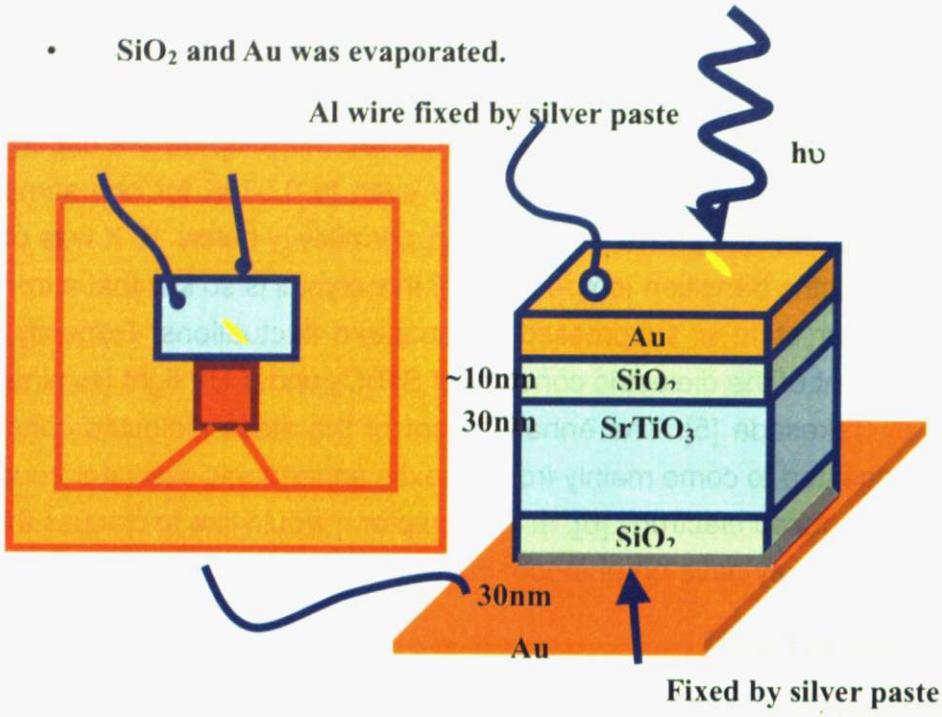

Fig.5-1 Geometry of the sample in capacitance measurements.

Results and discussion

Figure 5-2 shows the time dependence of photocurrent measured at different temperatures. The vertical axis shows the normalized photocurrent and the horizontal axis shows time. The purple thick broken line shows the light intensity. The chopping frequency was 1.4 Hz. The light intensity is not a perfect square wave because the optical chopper slit and the light beam diameter had similar sizes. Intermediate intensities occur when the chopper partially blocks the light beam. The excitation wavelength was 360 nm, which corresponds to 3.44 eV. Light intensity was ~ 1.0×10^{-2} mW/cm^2. From Fig. 5-2, it is clear that the photocurrent signal is delayed relative to the light intensity by 0.2~0.6 s, with delay time being different at each temperature. Initially, the response became slower with increasing temperature, with the slowest response occurring at around 35 K. At even higher temperatures, the response became faster again. The decay time was about 0.6~0.9 s, smaller than the current rise time, but with a minimum at around 35K. In order to compare the response at each temperature, the rise and decay times are plotted in Figure 5-3.

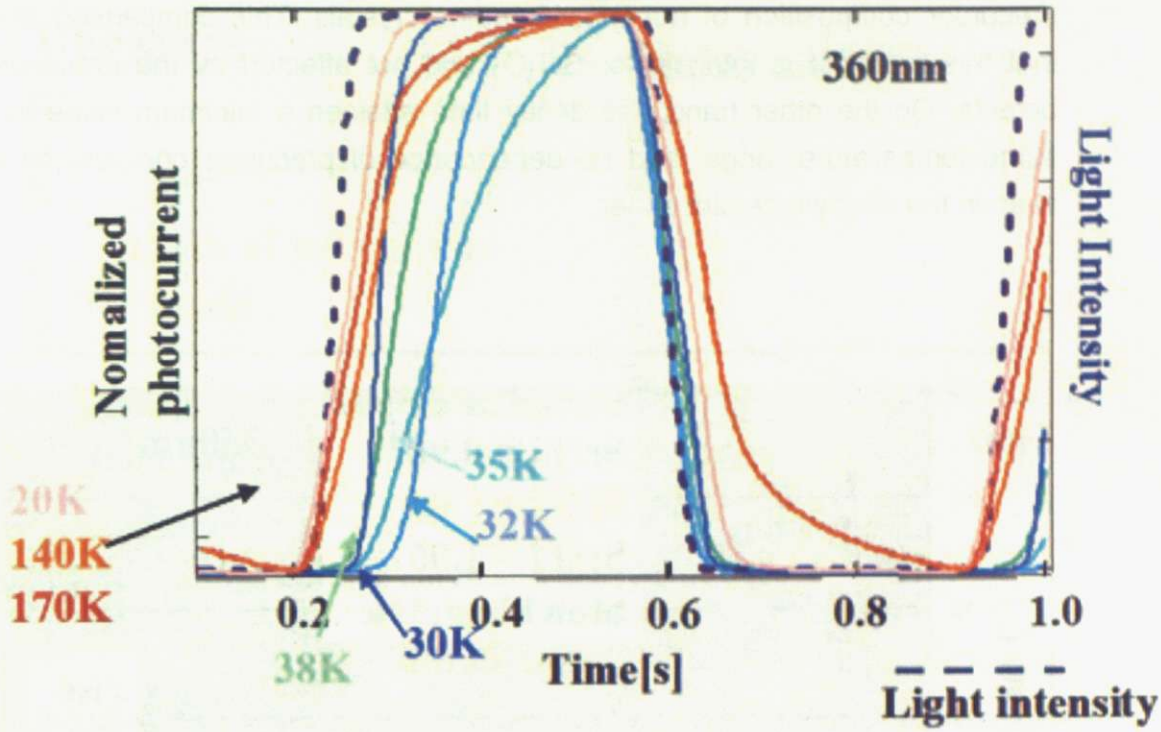

Fig.5-2 Time dependence of photocurrent of SrTiO3

Figure 5-4 show the models used to analyze the rise and decay curves. The rise time was defined as the time between the start of illumination and the time when the current attained 63% of the maximum current. The decay time was defined as τ in the follow equation.

$$I_{Ph} = C_0 + C_1(t - t_0) + A_0 \exp\left(\frac{-(t - t_0)}{\tau}\right), \qquad (5\text{-}1)$$

where I_{ph} is the photocurrent and C and A are constants. This equation comes from a general expression of the decay curve;

$$I_{Ph} = \sum_{i=1}^{M} A_i e^{-t/\tau_i} \qquad (5\text{-}2)$$

Eq. 5-1 is an approximation that only keeps the first component and the background of Eq. 5-2.

A sharp peak was seen in the rise time at low temperature in each plot. All samples showed the peak at around 35 K, independent of the Sr/Ti ratio in the

precursor composition of non-stoichiometric crystals. This comparison shows that this behavior is intrinsic for $SrTiO_3$ and not affected by the presence of defects. On the other hand, the decay time attained a minimum value in the same temperature range, and no dependence of precursor composition was seen in the decay time plot either.

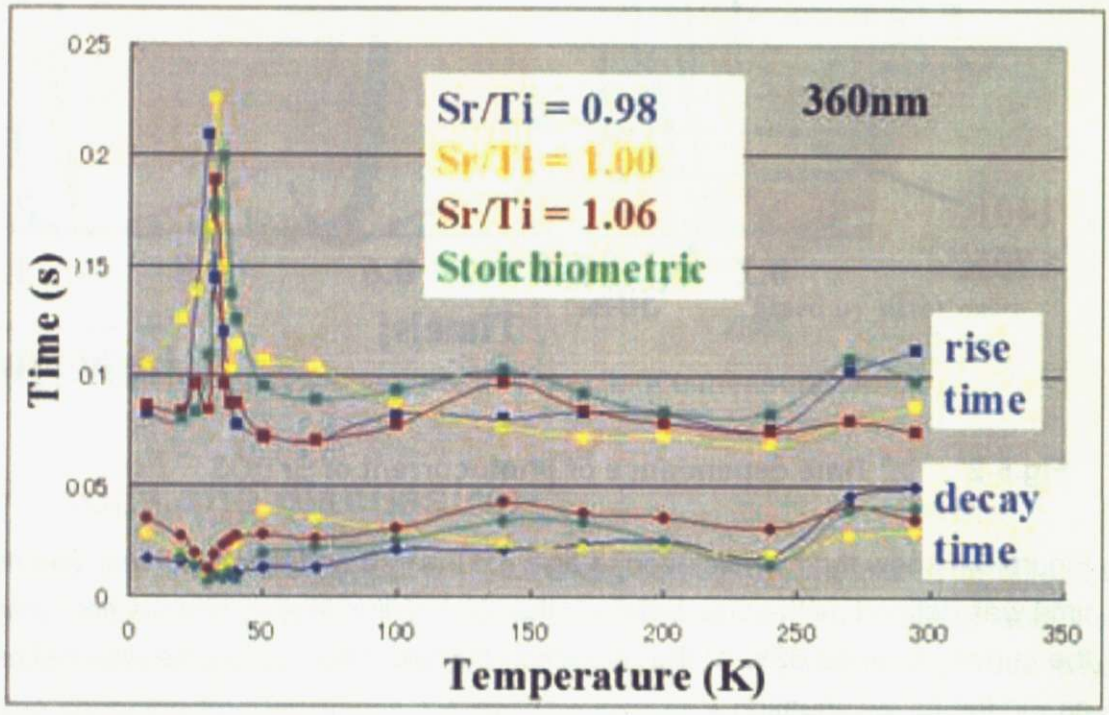

Fig.5-3 Rise time and decay time in each SrTiO3

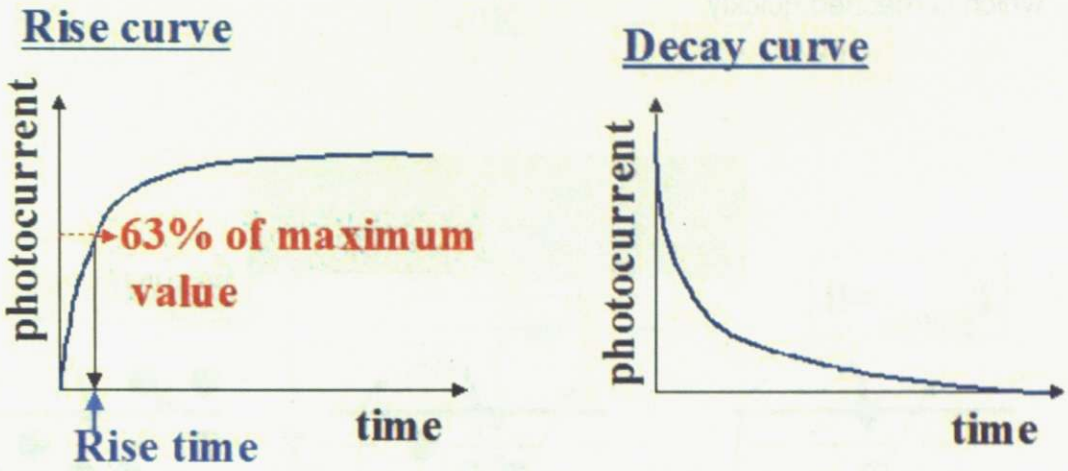

(a) (b)

Fig.5-4 Model of rise curve and decay curve

If the usual semiconductor picture is used to analyze the dynamic response of the photocurrent, a good starting point is a defect-rich system like CdSe. In that case, the delay in the current is caused by the presence of many trap sites which are caused by crystal defects. The delay is proportional to the time needed to fill the trap sites up to a steady-state equilibrium level. Fig.5-5 is the schematic model of the filling trap sites. The upper model explains how the trap sites are filled as a function of time. The lower model shows the experimental time dependence of photocurrent of $SrTiO_3$ at 35 K. There are no electrons in the conduction band just after the illumination start, because the electrons are immediately captured by the trap sites and cannot contribute to the measured current. As the trap sites are gradually filled by electrons, the rate of capturing electrons is gradually balanced by the rate of thermally releasing electrons from trap sites. As time advances, the number of electrons in the conduction band and trap sites are in equilibrium, but the time needed to reach the equilibrium is longer in a defect-rich crystal. The accumulation time is reflected in the photocurrent dynamics.

Considering the semiconductor model, a possibility reason for the observed temperature dependence of the rise time is as follows. In the high-temperature regime (Figure 5-6), the thermal energy that is available for releasing electrons from shallow trap sites is large, increasing the detrapping rate and therefore fewer electrons are captured by the trap sites even in the equilibrium state,

which is reached quickly.

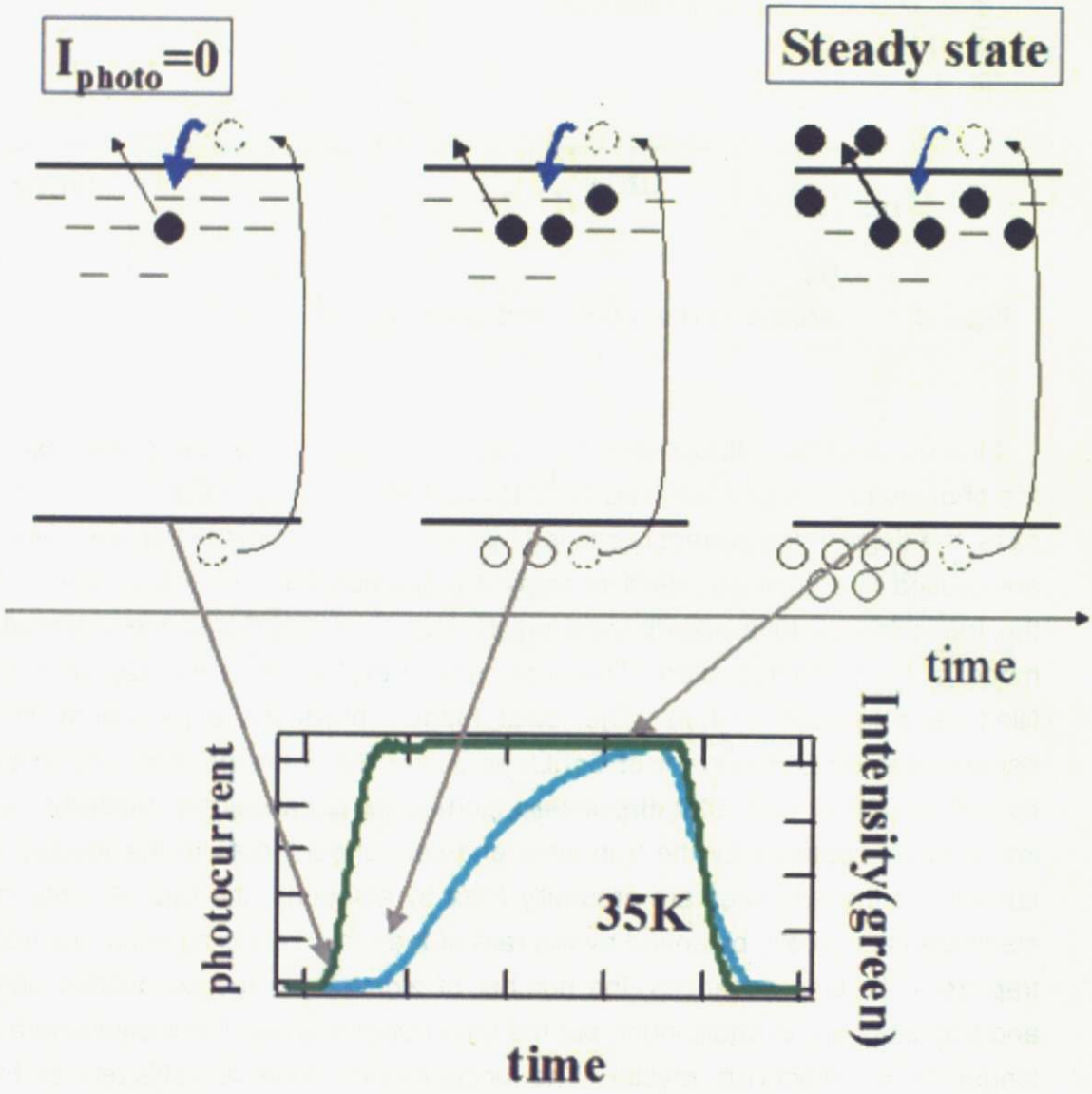

Fig.5-5 Schematic model of accumulating photo-excited carriers

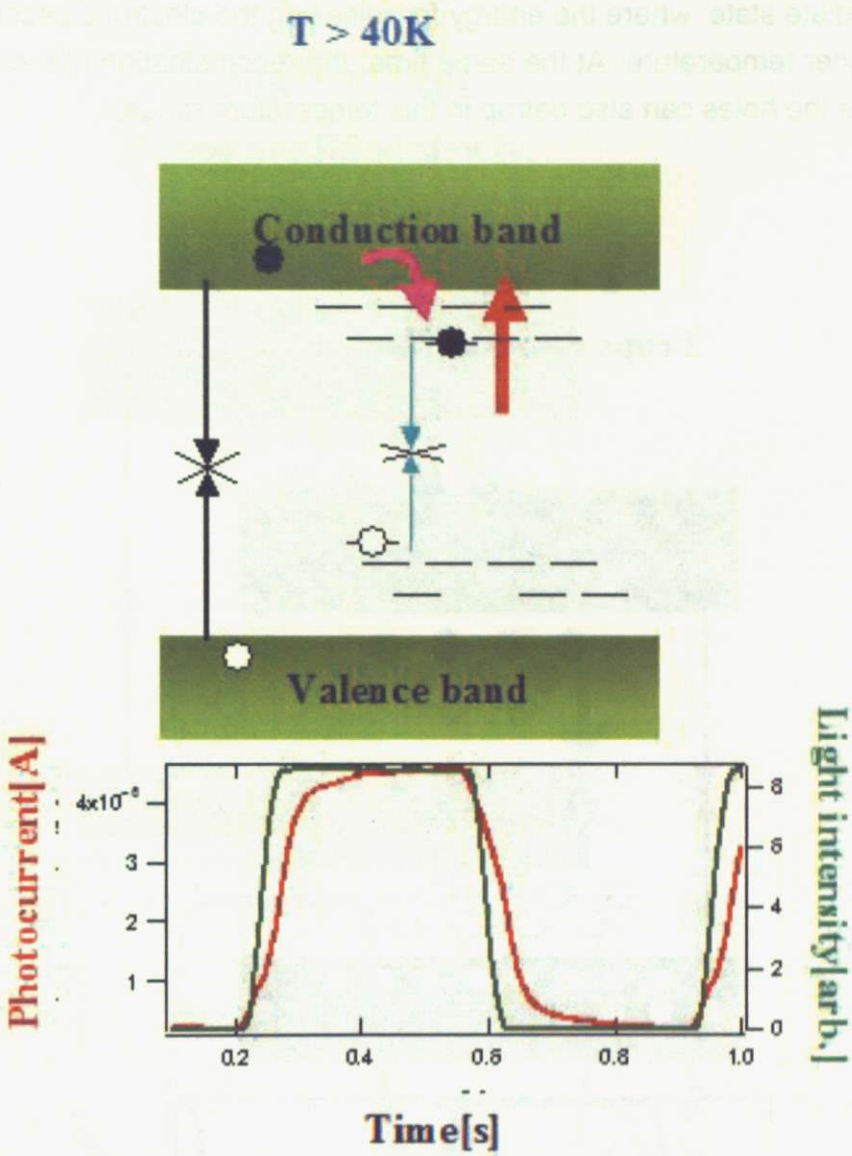

Fig.5-6 Schematic model of the behavior of photo-excited electron at T > 40 K.

In the low-temperature regime (Figure 5-7), trap sites would always remain filled by electrons because the energy for thermally releasing electrons from trap sites is low. At the light chopping frequency of 1.4 Hz, the trapped charge population would remain virtually unchanged. Under these conditions, any electrons excited by the light illumination remain in the conduction band and contribute to the photocurrent. The current is much higher at low temperature, because the holes also remain frozen, reducing the recombination rate.

In the region of 30 K < T < 40 K region (Figure 5-8), the system is in an

intermediate state, where the energy for releasing the electrons becomes higher with higher temperature. At the same time, the recombination rate change also, because the holes can also detrap in this temperature range.

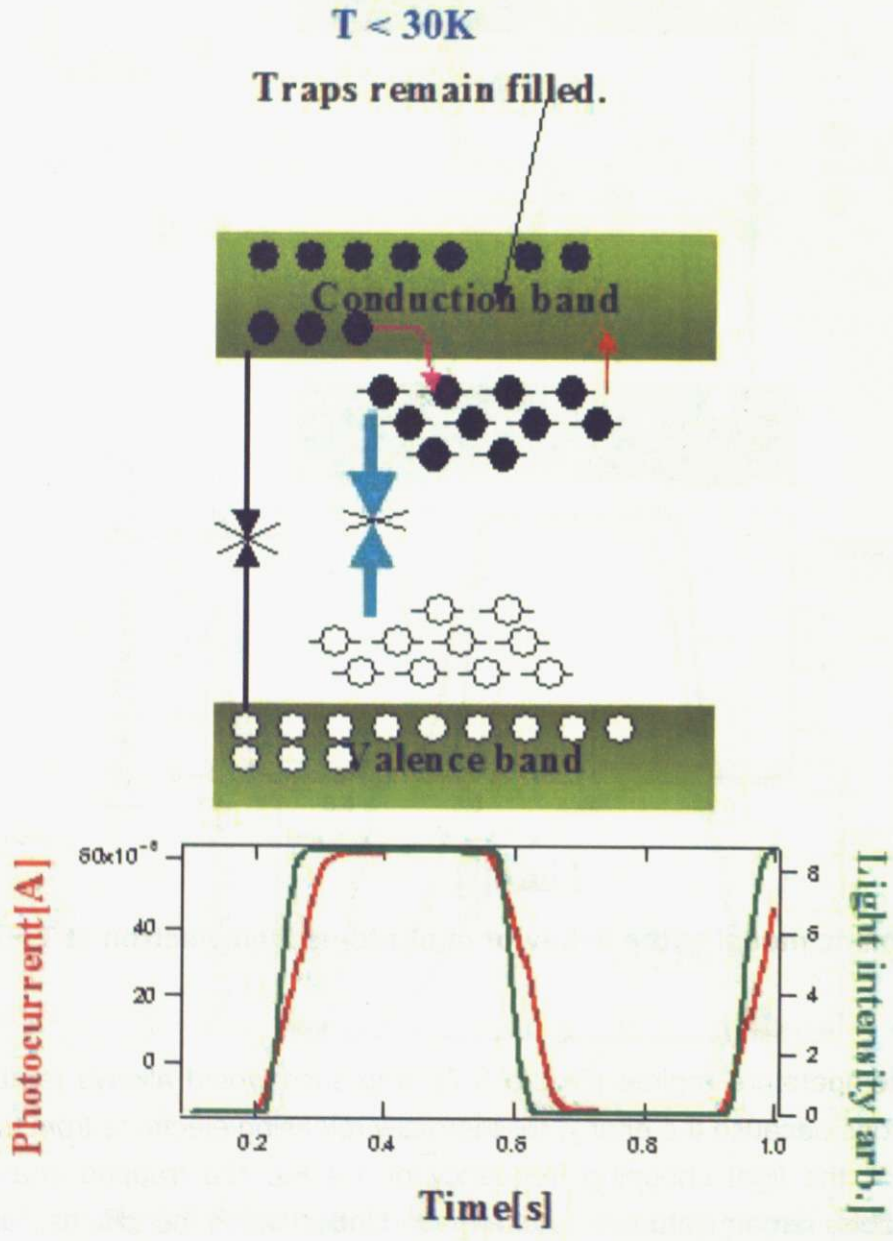

Fig.5-7 Schematic model of the behavior of photo-excited electrons at T < 30 K.

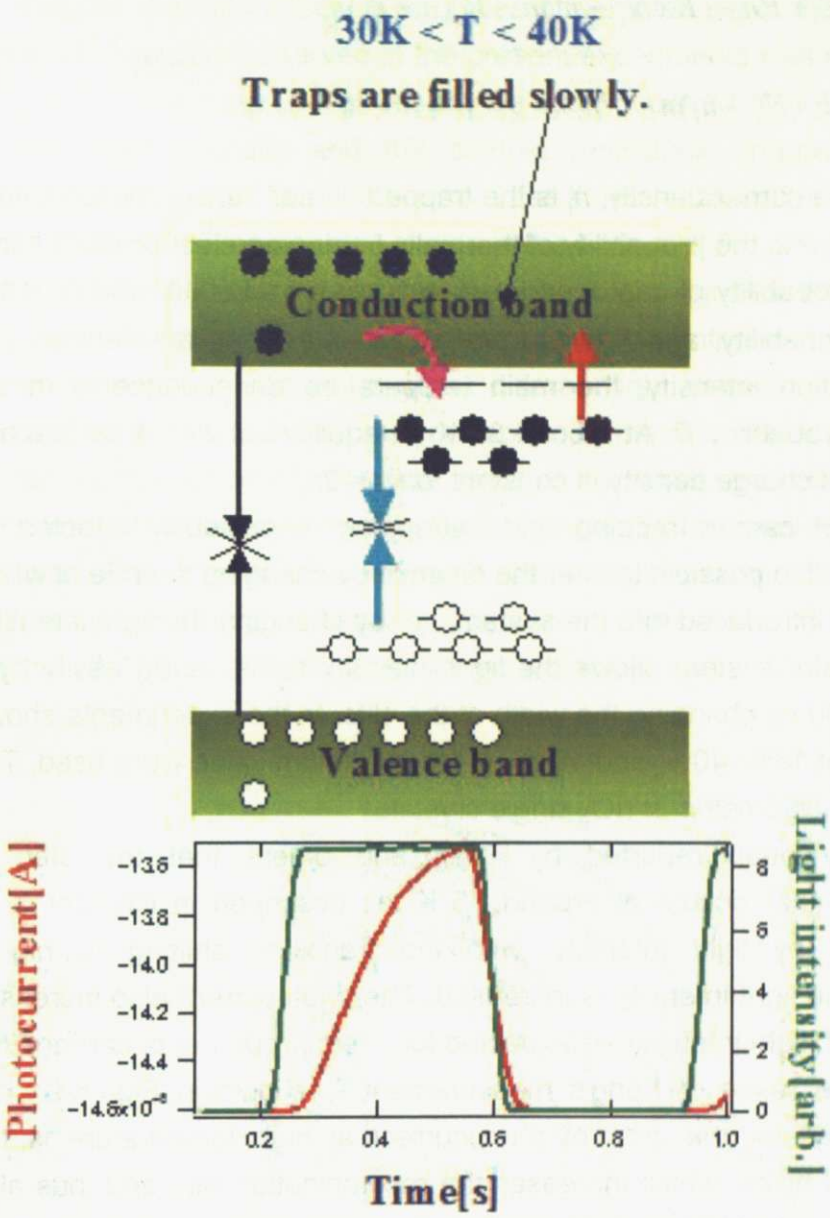

Fig.5-8 Schematic model of the behavior of photo-excited electrons at 30 K < T < 40 K.

The rate equations that describe the photocarrier dynamics can be written as follows:

$$\frac{dn}{dt} = F + Pn_t - R_t(N_t - n_t)n - R_r(n + n_t)n$$
$$\frac{dn_t}{dt} = R_t(N_t - n_t)n - Pn_t \qquad (5\text{-}3)$$

where n is the free carrier density, n_t is the trapped carrier density, N_t is the total trap state density, P is the probability of thermally freeing an electron from a trap state, R_t is the probability of capturing an electron in a trap state, and R_r is the recombination probability, and F is the probability of exciting an electron. For constant illumination intensity, the main temperature dependence is in the thermal freeing probability P. At around 35 K an equilibrium would be reached where the trapped charge density is constant, $dn_t/dt=0$.

The balance of carrier trapping and detrapping is obviously affected by temperature. It is also possible to alter the balance by changing the rate at which photocarriers are introduced into the system, i.e. by changing the light intensity. The monochromator system allows the light intensity to be varied easily by a factor of about 100 by changing the width of the slits. In the experiments shown here, intensities of 16%, 40%, and 100% of the maximum value were used. The samples were stoichiometric $SrTiO_3$ single crystals.

It has already been reported by Feng and others that the step in photoconductivity that occurs at around 35 K, as described in Chapter 3, is strongly affected by light intensity, with the transition shifting to higher temperature as the light intensity is increased. The photocurrent also increases systematically with light intensity, as expected for a larger number of carriers that is generated. The result of Feng's measurement is shown in Fig. 5-9. The explanation offered for the drop of photocurrent at high temperature is the freeing of trapped holes, which increases the recombination rate and thus also the observed current. However, the explanation that the recombination rate change is caused by freeing of holes as the Fermi level for electrons and the demarcation level for holes shifts away from the respective band edges is only justified by the assumption that the crystal is unintentionally doped by Fe impurities, which act as acceptor-type hole trap sites. Although the samples used in this work do not contain excessive Fe impurities, similar photoconductivity was observed in nonstoichiometric crystals, in which the density of Sr vacancies, which can act as similar acceptor sites, would be expected to vary over a wide range. However, no major differences were seen

between the nonstoichiometric crystals.

Despite the differences in the types of samples used, the general excitation intensity behavior observed in the present experiments was similar, as shown in Fig. 5-10. The jump to high-resistance state occurred at higher temperature for higher light intensity and the sample resistance dropped over the whole temperature range. The photocurrent rise times measured for the same samples with same condition are also shown in the bottom of Fig. 5-10. It is clear that the rise time peak tracks the resistance jump without significant change in shape.

A model that can be used to understand the photoresistance behavior in the intermediate temperature range for different light intensities is illustrated in Fig. 5-11. The pink-colored arrows correspond to the rate of electron capture by trap sites. At the temperature where most of the holes are captured at trap sites, photo-excited electrons mostly remain the conduction band and the photocurrent is high. The number of electrons in the conduction band depends on the light intensity. Under higher-intensity illumination, both P and R_t in eq. 5-3 become larger and, thus, a higher temperature would be needed for equilibrium.

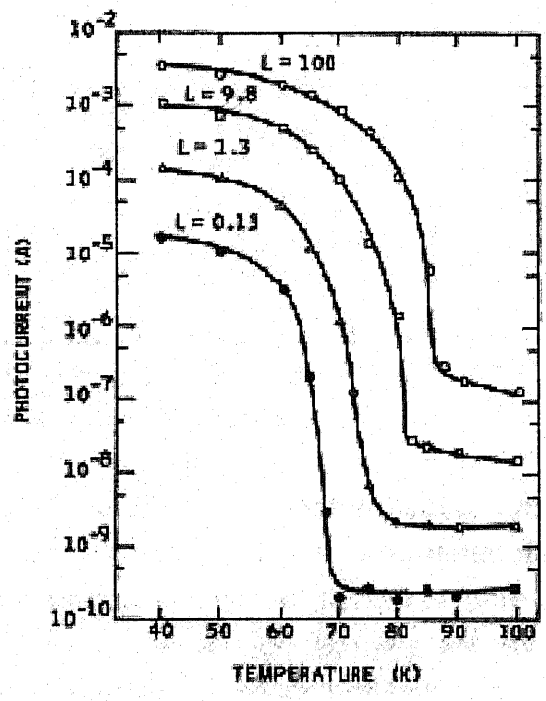

Fig.5-9 Temperature dependence of photocurrent under several intensities of UV illumination.

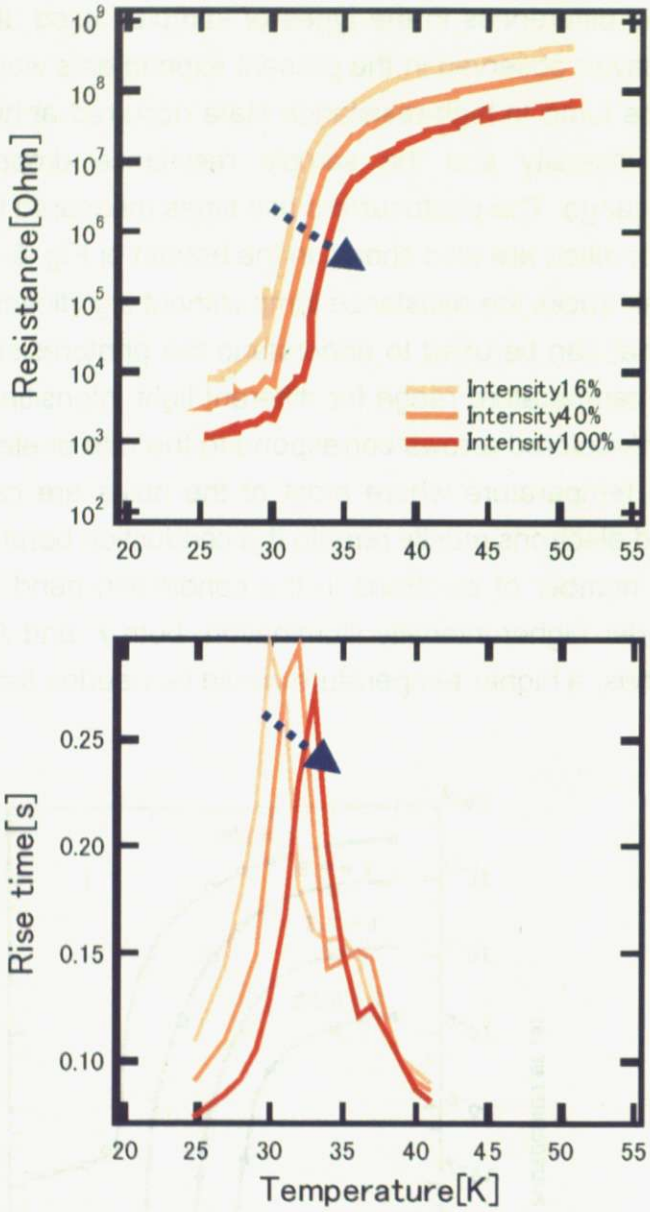

Fig.5-10 Temperature dependence of resistance and rise time under different intensity illuminations.

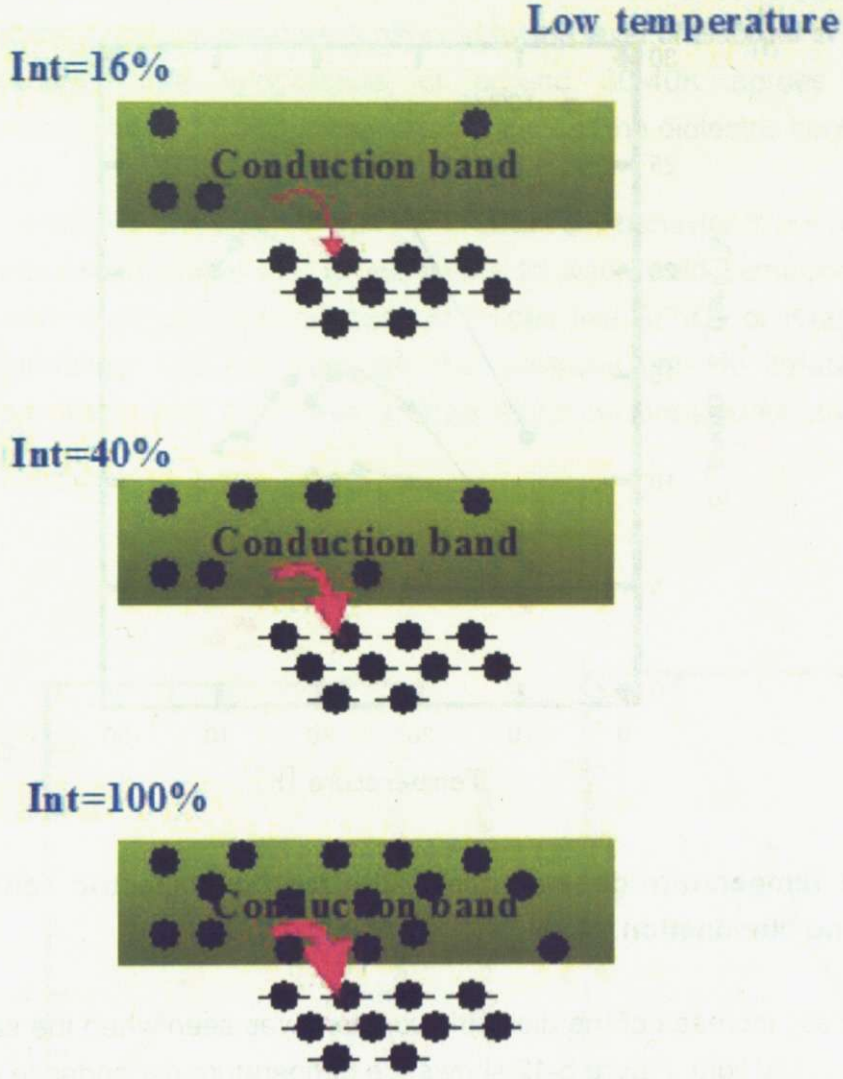

Fig.5-11 Model of electron behavior under different intensities of illumination at low temperature.

Although the trapping model discussed above can, at least qualitatively, describe the observed photoconductivity behavior, there are also a number of open questions. The above model requires the presence of acceptor-type hole trapping centers, since the large photoconductivity change is presumably related to carrier recombination, driven by hole delocalization at high temperature. In order to probe the significance of other mechanisms, the dielectric constant ε of a stoichiometric $SrTiO_3$ sample was measured close to the transition

temperature of 35 K.

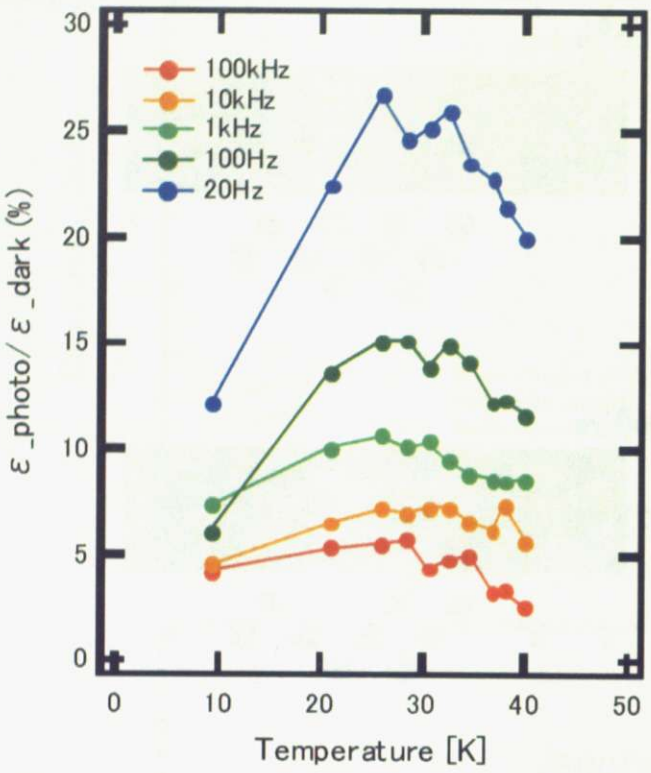

Fig.5-12 Temperature dependence of the ratio of dielectric constant with UV and no illumination.

A systematic increase of the dielectric constant was seen when the sample was exposed to UV light. Figure 5-12 shows the temperature dependence of the ratio of dielectric constant with and without UV light for different measurement frequencies. A peak in the enhancement of the dielectric constant was seen at the transition temperature. The ε_{dark}, measured without UV light is plotted in Fig. 5-13, showing the characteristic critical temperature at about 35 K, which coincides with the large change in photoconductivity discussed earlier. These dark behavior coincides with earlier published work, as shown in Fig. 5-14 [4] [8].

For a normal ferroelectric, the zero intercept of the $1/\varepsilon$ plot would point at the transition temperature where ferroelectric ordering sets in. Although this does not happen in $SrTiO_3$, it is possible to distort the crystal and that way induce ferroelectricity. One technique that has been used for this purpose is oxygen isotope substitution, which has been shown to result in ferroelectric $SrTiO_3$ crystals below 30 K. The peak point in top-right picture of fig. 5-14 is the

transition point. Comparison of samples with different isotope substitution ratios shows that the Curie temperature is affected by the level of disorder in the crystal. The observed Curie temperature of around 30-40K agrees with the enhancement of rise time and photoenhancement of the dielectric constant seen in this study.

These considerations suggest that the conductivity behavior is not related to a simple defect-state model that is applicable to disordered semiconductors. A possible source of carrier localization in oxides like $SrTiO_3$ or $KTaO_3$ is also polaron formation. Qiu has reported that polarons can be created by UV illumination, which can also have a large effect on photoconductivity at low temperature [6].

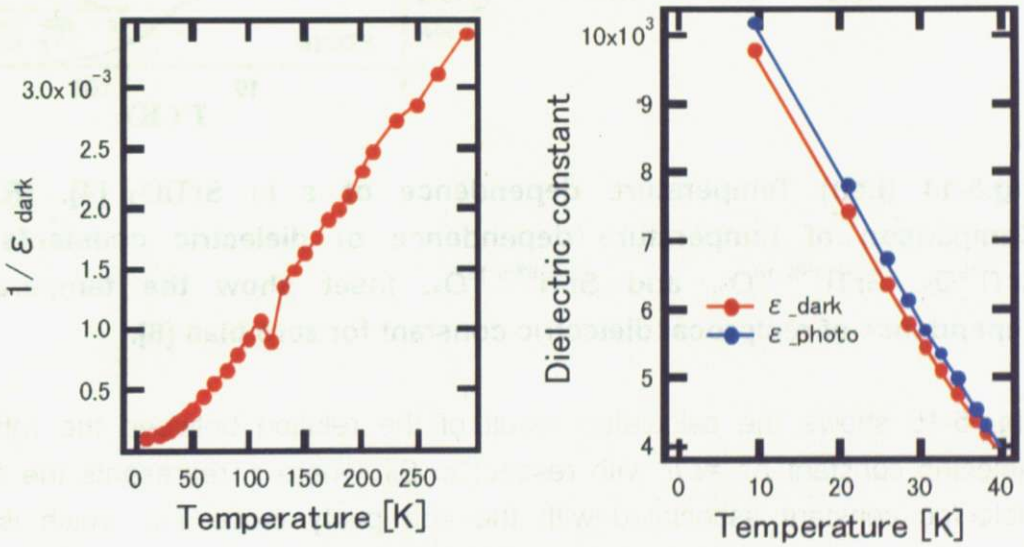

Fig.5-13 (Left) Temperature dependence of 1/ε with no illumination. (right) Temperature dependence of ε at low temperature with and without UV illumination. Measurement frequency is 100MHz.

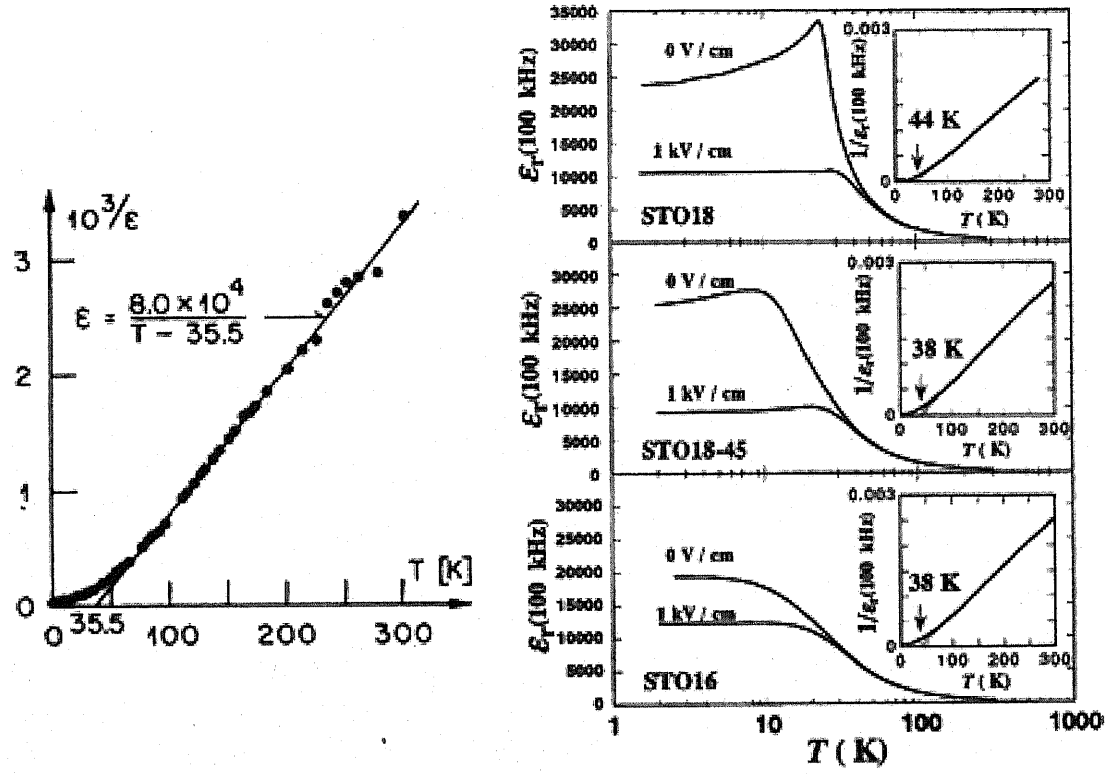

Fig.5-14 (Left) Temperature dependence of ε in $SrTiO_3$ [4]. (Right) Comparison of temperature dependence of dielectric constants for $SrTi^{16}O_3$, $SrTi^{45\%\text{-}18}O_3$, and $SrTi^{93\%\text{-}18}O_3$. Inset show the temperature dependence of reciprocal dielectric constant for zero bias [8].

Fig. 5-15 shows the calculated result of the relation between the ratio of dielectric constant $\Delta\varepsilon = \varepsilon'/\varepsilon$ with respect to S_d, where ε' represents the static dielectric constant associated with the odd parity mode T_{1u}, which is the dominant mode in UV-illuminated $SrTiO_3$ at low temperature. S_d is the dimensionless constant of quadratic coupling strength between the electrons and the site-localized T_{1u} mode.

It can be considered that the electron-T_{1u} mode coupling is responsible for the localization of carriers, since the effective mass of a polaron can be very large. Such localization mechanism can also affect the recombination rate and thus the conductivity of the sample. Such a mechanism would occur in $SrTiO_3$ regardless of the presence of defects and would explain why a similar low-temperature conductivity behavior was seen even in samples that were intentionally defect rich.

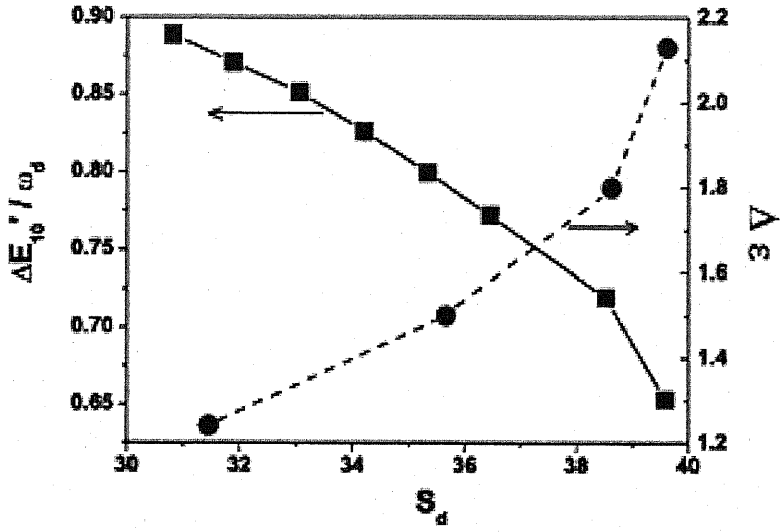

Fig.5-15 Circle indicates dielectric ratio Δε with respect to S_d [6]. S_d is the dimensionless constant of quadratic coupling strength between the electrons and the site-localized T_{1u} mode.

Conclusion

Photoconductivity dynamics and dielectricity of UV-illuminated $SrTiO_3$ was discussed in this chapter. There was characteristic temperature around 35K, where large delay of rise time happened and higher enhancement of dielectricity. The dynamics was not sample dependent, so it can be considered that the dynamics is intrinsic behavior of $SrTiO_3$. The large jump of resistivity which is also seen in chanter 3,4 was seen under different intensity of illumination, but at different temperature. It was clear that the high jump of resistivity and delay happen at the same temperature. I assumed that one possibility is the existence of a large trap state density, which changes the dynamic balance between the recombination rate and carrier trapping. The second possibility is a dielectric coupling between lattice vibrations and carriers in photo-excited $SrTiO_3$.

References

1. H. Bube. Photoconductivity of solids, 285
2. T. E. Murphy, K. Moazzami, and J. D. Phillips, J. Elec. Matt. **35**, 543 (2006).
3. P. A. Fleury and J. M. Worlock, Phys. Rev. **174** 613 (1968).
4. K. A. Muller, H. Burkard, Phys. Rev. **B 19**, 3593 (1979).
5. M. Takesada, T. Yagi, M. Itoh, and S. Koshihara, J. Phys. Soc. Jpn. **72**, 37 (2003).
6. Y. Qiu, C. Q. Wu, and K. Nasu, Phys. Rev. **B 72**, 224105 (2005).
7. T. Feng, Phys. Rev. B **25**, 627 (1982).
8. M. Itho, R. Wang, Y. Inaguma, T. Yamaguchi, Y-J. Shan, and T. Nakamura, Phys. Rev. Lett. **82**, 3540 (1999).

Chapter 6

Summary and Conclusions

I investigated the relation between crystal defects and photoconductivity in $SrTiO_3$. In Chapters 1 and 2, I presented a general introduction of oxide electronics, purposes of this study, and described the measurement systems used in this study.

In Chapter 3, influence of surface damage from manufacturing process on the transport properties was discussed. Crystal damage from the growth process or the polishing process may damage the surface layer of a substrate crystal and this effect was indeed seen in photoconductivity measurements as an increase of the band tail at low temperature. No significant effect was seen in temperature dependence of photoconductivity. The cleaved surface can be considered as a good quality reference surface in terms of defect density on the crystal surface.

In Chapter 4, I discussed samples that intentionally made defect rich. One method for generating defects is high-temperature annealing. Clear Sr segregation was observed on the surface of annealed $SrTiO_3$ crystals. Defects were induced only near the surface layer in annealed samples, so differences were seen in only with deep UV illumination, which is more surface sensitive. The resistivity tended to be larger with higher temperature annealing. Annealing temperature dependence of defect density is difficult to discuss in photocurrent measurement, so another investigation is needed to study this effect further. The other method for inducing defects was controlling the precursor powder ratio in bulk crystal growth. Deviation from the stoichiometric composition resulted in higher defect density in the final crystals, which could be seen as a change in the absolute value of photoconductivity, and the height of the photoresistance transition at around 30K. In photon energy dependence measurement, a band tail was seen in near stoichiometric samples. The reason for this is not clear but several kinds of defects may be generated in the crystal and complicated carrier behavior can be caused by the deviation of the raw material from the ideal composition. In Chapter 5, photocurrent dynamics and dielectric properties under UV illumination were discussed. A large slowdown of the photocurrent response was seen in a narrow temperature range close to the conductivity transition. A peak in the photoinduced dielectric enhancement was seen in the same temperature range. The characteristic temperature where the slow

dynamic response occurs changed with light intensity. To possible sources for the observed behavior were considered. One possibility is the existence of a large trap state density, which changes the dynamic balance between the recombination rate and carrier trapping. The second possibility is a dielectric coupling between lattice vibrations and carriers in photo-excited $SrTiO_3$.

Acknowledgement

This work was done at the Institute for Solid State Physics of University of Tokyo from April 2006 to January 2008.

First of all, I would like to express my deepest gratitude to Professor Mikk Lippmaa Mere words could never express my gratitude, yet I will try to explain how grateful I am for everything that you have done. Valuable and accurate help of my work, instruction of presentation, and introduction of much of knowledge of physics are all helpful for my life as graduated student.
I would like to thank to Dr. Tsuyoshi Ohnishi. I often supported his novel ideas, appropriate instruction about instruments, and his encouraging. His attitude for work was good polestar for my student life. Mr. Shinya Meguro provided me good tool for comfortable study. Prof. Ichiro Takeuch, Dr. Matvejeff Mikko, and Dr. Kang Sookil gave me fruitful talks. Dr. Keisuke Shibuya, Mr. Hiromasa Kondo, Taisuke Sato gave me useful advices, good instructions, and discussed a lot about my work. Mr. Kazunori Nishio and Mr. Takuya Abe were best colleague for my Kashiwa life. Thank you for meaningful 2 years with you.

I will also thank to secretaries Junko Kawamura, Rie Takahashi, Akiko Ono and Yukiko Hanada for office work and encouragement. Your support for our work made part of our investigations. I'll give my acknowledgements to all my friends for their encouragement and support in Kashiwa.

Finally I would like to express my sincere gratitude to my family for their endless support and love in all means.

29 Jan. 2008
Yasufumi Urata